Biomaterials 291 (2022) 121865

Contents lists available at ScienceDirect

Biomaterials

journal homepage: www.elsevier.com/locate/biomaterials

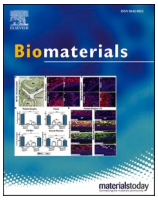

Rhamnan sulfate reduces atherosclerotic plaque formation and vascular inflammation

Nikita P. Patil [a,1], Almudena Gómez-Hernández [b,1], Fuming Zhang [c], Limary Cancel [d], Xu Feng [a], Lufeng Yan [c], Ke Xia [c], Eri Takematsu [a], Emily Y. Yang [a], Victoria Le [a], Megan E. Fisher [a], Agueda Gonzalez-Rodriguez [e], Carmelo Garcia-Monzon [e], James Tunnell [a], John Tarbell [d], Robert J. Linhardt [c], Aaron B. Baker [a,f,g,h,*]

[a] Department of Biomedical Engineering, University of Texas at Austin, Austin, TX, USA
[b] Department of Biochemistry and Molecular Biology, School of Pharmacy, Complutense University of Madrid, Madrid, Spain
[c] Departments of Chemistry and Chemical Biology, Chemical and Biological Engineering, Biology, and Biomedical Engineering, Center for Biotechnology and Interdisciplinary Studies, Rensselaer Polytechnic Institute, Troy, NY, USA
[d] Department of Biomedical Engineering, The City College of New York, CUNY, New York, NY, USA
[e] Liver Research Unit, Hospital Universitario Santa Cristina, Instituto de Investigación Sanitaria Hospital Universitario de La Princesa, CIBERehd, Madrid, Spain
[f] Institute for Cellular and Molecular Biology, University of Texas at Austin, Austin, TX, USA
[g] The Institute for Computational Engineering and Sciences, University of Texas at Austin, Austin, TX, USA
[h] Institute for Biomaterials, Drug Delivery and Regenerative Medicine, University of Texas at Austin, Austin, TX, USA

ARTICLE INFO

Keywords:
Rhamnan sulfate
Marine polysaccharides
Atherosclerosis
NF-κB pathway
Inflammation

ABSTRACT

Objective: While lipid-lowering drugs have become a mainstay of clinical therapy these treatments only slow the progression of the disease and can have side effects. Thus, new treatment options are needed to supplement the effects of lipid lowering therapy for treating atherosclerosis. We examined the use of an inexpensive and widely available marine polysaccharide rhamnan sulfate as an oral therapeutic for limiting vascular inflammation and atherosclerosis.

Methods and results: We found rhamnan sulfate enhanced the barrier function of endothelial cells, preventing the deposition of LDL and maintaining barrier function even in the presence of glycocalyx-degrading enzymes. Rhamnan sulfate was also found to bind directly to FGF-2, PDGF-BB and NF-κB subunits with high affinity. In addition, rhamnan sulfate was a potent inhibitor of NF-κB pathway activation in endothelial cells by TNF-α. We treated ApoE$^{-/-}$ mice with a high fat diet for 4 weeks and then an addition 9 weeks of high fat diet with or without rhamnan sulfate. Rhamnan sulfate reduced vascular inflammation and atherosclerosis in both sexes of ApoE$^{-/-}$ mice but had a stronger therapeutic effect in female mice. Oral consumption of rhamnan sulfate induced a significant decrease in cholesterol plasma levels in female mice but not in male mice. In addition, there was a marked reduction in inflammation for female mice in the liver and aortic root in comparison to male mice.
Conclusions: Rhamnan sulfate has beneficial effects in reducing inflammation, binding growth factors and NF-κB, enhancing endothelial barrier function and reducing atherosclerotic plaque formation in ApoE$^{-/-}$ mice.

1. Introduction

Cardiovascular disease continues to be a major cause of mortality worldwide, with roughly 17 million people dying from cardiovascular disease worldwide each year and an associated healthcare cost of over $500 billion in medical costs annually. Atherosclerosis is a chronic, progressive disease in which the accumulation of lipids, endothelial dysfunction and inflammatory processes within the vascular wall lead to plaque development [1,2]. Atherosclerotic plaques underlie a many forms of vascular disease and can lead to organ ischemia, stroke and myocardial infarction. Pharmacotherapy with statins have become a mainstay of modern treatment of atherosclerosis but often only slow the

* Corresponding author. University of Texas at Austin Department of Biomedical Engineering 1 University Station BME 5D, C0800 Austin, Austin, TX, USA.
E-mail address: abbaker1@gmail.com (A.B. Baker).
[1] Denotes equal contribution.

https://doi.org/10.1016/j.biomaterials.2022.121865
Received 4 December 2021; Received in revised form 9 September 2022; Accepted 17 October 2022
Available online 28 October 2022

inevitable progression of the disease and do not represent a cure for the vast majority of patients [3,4].

The endothelial glycocalyx is a layer of glycans that lines the interior of the artery and interacts with the flowing blood [5]. The endothelial glycocalyx provides an atheroprotective effect within the artery, in part by maintaining the endothelial barrier function that prevents lipid deposition, reduces inflammation, and lowers the risk of arteriothombosis [6–8]. During the progression of atherosclerotic disease, there is loss of the glycocalyx [9] and associated lipid deposition, and inflammation [10,11]. Many of the major risk factors for atherosclerosis, including elevated C-reactive protein, hyperglycemia, oxidized lipids, and hyperlipidemia, lead to the depletion and degradation of the endothelial glycocalyx [12–17]. Major components of the glycocalyx include glycosaminoglycans, including heparan sulfate, chondroitin sulfate and hyaluronic acid. In the absence of these glycosaminoglycans, endothelial barrier function is compromised and immune cell adhesion is increased [18–20].

Many marine product-derived polysaccharides have a structure roughly analogous to the polysaccharides in the glycocalyx and have oral bioavailability [21,22]. Several of these compounds including laminarin sulfate and fucoidan have been explored as treatments for vascular disease and as anti-coagulants [22]. Sulfated polysaccharides specifically have exhibited anti-oxidant and anti-inflammatory properties making them potential therapeutics for atherosclerosis [23]. Rhamnan sulfate (RS) is a polysaccharide derived from green seaweeds including *Monostroma nitidum*. Rhamnan sulfate has a structure similar to endogenous glycosaminoglycans but is composed of a different backbone of polysaccharides which are primarily alpha-1,3-linked L-rhamnose residues that have sulfate groups. Thus, RS provides a rough approximation of the chemical structure of many of the glycans that compose the endogenous glycocalyx of the artery including that of heparan sulfate [24]. Rhamnan sulfate has been shown to decrease inflammation in vascular endothelial cells in vitro and inhibit hepatic lipogenesis in a zebrafish model [25,26]. These properties make RS a promising candidate as an oral treatment for atherosclerosis.

In this work, we examined the use of highly purified RS as a potential therapy for plaque development and vascular inflammation. Our work demonstrates that RS has an anti-inflammatory effect on endothelial cells, can bind to NF-κB and inhibit inflammatory signaling. In addition, we found that RS can directly bind to PDGF-BB and inhibit its effects on vascular smooth muscle cell (vSMC) migration and proliferation. We further tested RS as an oral therapy for atherosclerosis in male and female ApoE$^{-/-}$ mice. We found that RS reduced atherosclerosis in both sexes, but it had stronger lipid lowering and anti-inflammatory effects on female mice in comparison to male mice. Taken together, our results support that RS has potential as an inexpensive oral treatment for atherosclerosis and may have potential for treating nonalcoholic fatty liver disease in female patients.

2. Methods

Cell culture. Human umbilical vein endothelial cells (HUVECs) were purchased from PromoCell. They were grown in MCDB-131 culture medium (Life Technologies) with EGM-2 growth factors (R&D Systems), 10% fetal bovine serum (FBS), L-glutamine and antibiotics. Human aortic smooth muscle cells (HAoSMCs) were grown in MCDB-131 culture medium (Life Technologies) with 10% FBS, L-glutamine and antibiotics. Cells were received at passage 2 and were not allowed to grow past passage 8. Human coronary artery endothelial cells (HCAEC) were purchased and grown in cell specific growth medium according to the manufacturer's instructions (Cell Applications). All cells were grown at 37 °C with 5% CO_2.

Rhamnan sulfate purification/analysis. Rhamnan sulfate was isolated from green seaweed (Monostroma nitidium sourced from Japan) powder using methods described previously [27]. The powder was homogenized in distilled water (1:30 seaweed:water) and extraction was performed at 100 °C for 3 h. The extract was centrifuged at 4700*g* for 10 min and the supernatant was collected. Ethanol was added to the supernatant to achieve 80% ethanol per total volume. Crude polysaccharide was precipitated from the supernatant with three volumes of anhydrous ethanol and dissolved in distilled water. The polysaccharide solution was dialyzed in a cellulose membrane (molecular weight cut-off of 3500 Da) against distilled water for three successive days. After dialysis, the RS was lyophilized and weighed. Molecular weight of a monomer of RS was 150 kDa, measured after purification, and the aggregate in 1 mg/mL solution was estimated to be 2.67×10^7 kDa using DLS.

Labeling of RS with FITC. Labeling and detection of RS with FITC was performed as described previously [28]. Briefly, the polysaccharide was activated by adding CNBr (8.33 mg/mL) to RS (20 mg/mL) with the mixture maintained at pH 11. Activated RS was desalted using a 20 cm Sephadex G-50 column in 0.2 M sodium borate (pH 8.0). The RS containing fractions were pooled and reacted with 2 mg fluoresceinamine. Gel filtration was used to separate RS-FITC from unreacted fluoresceinamine and the concentration of fluorescein determined by reading absorbance at 440 nm. Concentration of RS was determined using the phenolsulfuric acid method. Degree of addition was expressed as moles of fluorescein per mole of monosaccharide and molecules of fluorescein per polysaccharide molecule.

Inhibition of uptake pathways. Endothelial (HUVECs) and vascular smooth muscle cells (HAoSMCs) were grown to confluence in MCDB-131 medium as described earlier. To prevent mitosis, mitomycin (1 mg/mL; Sigma-Aldrich) was added to the cells, with no treatment cells as control. To prevent uptake through the caveolin mediated endocytosis pathway, nystatin (1 mg/mL; Thermo Fisher Scientific) was added to the cells, using DMSO (1 mg/mL) for control. Pitstop 2 and pitstop 2 negative control (1 mg/mL; Abcam) were added to both cell types to prevent uptake through the clathrin mediated endocytosis pathway. Rottlerin (1 mg/mL; Santa Cruz Biotechnology) and DMSO control were used to test for inhibition of macropinocytosis. All groups received 1 mg/mL RS labeled with FITC. Cells were fixed after treatments for 24, 48 and 72 h, stained with DAPI and imaged using a confocal microscope. Total uptake was calculated by averaging intensity for all cells. Nuclear uptake was calculated by averaging intensity of nuclei that were positive for FITC.

Proliferation and migration assays. To measure proliferation, cells (HUVECs or HAoSMCs) were seeded on a fibronectin coated 96-well plate and grown to confluence. They were starved with 0.5% FBS medium for 24 h, then treated with RS (100 or 1000 μg/mL) and growth factors (10 ng/mL PDGF-BB or FGF-2) for 72 h. Proliferation was measured using the BrdU Cell Proliferation Assay Kit (Cell Signaling Technology). Migration was measured using the ORIS Cell Migration Assay Kit (Platypus Technologies). Cells were seeded on a fibronectin coated ORIS plate and grown to confluence. The cells were then placed in media with 0.5% FBS for 24 h. The stoppers were removed, and the cells were treated with RS (100 or 1000 μg/mL) and growth factors (10 ng/mL PDGF-BB or FGF-2). Images of each well were captured every 24 h for the duration of the experiment using a Cytation 5 Cell Imaging Multi-Mode Reader (BioTek).

LDL permeability assay. Human coronary artery endothelial cells (HCAEC) at passages 4–8 were plated onto fibronectin coated Transwell membranes (12 mm diameter, 0.4 μm pores, Corning) at a density of 0.5×10^4 cells/cm^2. Cells reached confluence within 2–3 days after plating, and experiments were carried out on monolayers 4–6 days post-plating. Immediately before the start of an experiment the media was changed to the experimental media consisting of phenol-red free basal media (Cell Applications) supplemented with 1% bovine serum albumin (BSA; Sigma-Aldrich). For studies with treatments, the HCAECs were incubated with growth media (control) or growth media containing RS at 25 μg/mL for 24 h, followed by a 2 h incubation with Heparinase III (HepIII; Ibex pharmaceuticals, Quebec, Canada) at 135 mU/mL or 1215 mU/mL in experimental media. After the 2 h HepIII treatment, HCAECs were

rinsed twice with experimental media and the permeability of DiI-LDL was measured. Tumor necrosis factor alpha (TNF-α, 20 ng/mL; Sigma-Aldrich) and cycloheximide (chx, 3 mg/mL; Sigma-Aldrich) were used to induce elevated apoptosis and permeability [29]. The cells were grown for 5 days before incubation with TNF-α and chx (TNF-α/chx) in the presence or absence of the RS isoforms or heparin (100 μg/mL; Sigma-Aldrich). TNF-α/chx was removed after 3.5 h of incubation and the cells were allowed to recover for 20 h in the presence or absence of RS or heparin.

The experimental apparatus used for measurement of LDL was as described previously [29,30]. The apparatus consists of eight Delrin® chambers, each connected to a laser excitation source and an emission detector. A Transwell filter containing the HCAEC monolayer was inserted and sealed within the transport chamber creating a luminal (top) and abluminal (bottom) compartment. At the beginning of each experiment DiI-LDL (5 mg/mL; Biomedical Technologies) was added to the luminal compartment. The fluorescent detection system was then used to measure the solute concentration in the abluminal compartment of each chamber as a function of time. Each transport experiment consisted of a 1-h equilibration period, followed by application of a 10 cm H_2O pressure differential and data collection for 1 h. The permeability was calculated as.

Where $\Delta C_a/\Delta t$ is the change in the abluminal concentration with respect to time, V_a is the fluid volume in the abluminal compartment, C_1 is the concentration in the luminal compartment, and A is the area of the filter.

Immunostaining of heparan sulfate. Monolayers of HCAEC grown in Transwell membranes were stained for heparan sulfate using mouse monoclonal *anti*-heparan sulfate antibody (10E4 epitope, 1:100 in 2% goat serum, AMSBIO) following previously established protocols [31]. Briefly, monolayers were fixed in 2% paraformaldehyde and 0.1% glutaraldehyde in PBS for 30 min, blocked with 2% GS for 30 min, and incubated with primary antibody overnight at 4 °C in a humidified chamber. Monolayers were then rinsed and incubated with secondary antibody Alexa Fluor 488 goat anti-mouse IgG (1:300 in 2% GS) for 1 h at room temperature, and counterstained with DAPI. The stained monolayers were imaged using a ZEISS LSM 510 confocal microscope. ImageJ was used to quantify image intensity. The coverage of heparan sulfate was analyzed using the methods described in previous work [31].

Preparation of subendothelial matrix samples. Monolayers of HCAECs were grown for 14 days in Transwell filters before the cells were removed by a method shown to leave intact subendothelial matrix attached to the Transwell [32]. Briefly, the monolayers were washed three times in PBS, incubated in 20 mM NH_4OH in 0.1% Triton X-100 for 5 min at room temperature, washed three times in PBS, and washed three times in basal media containing 3% BSA. The filters with subendothelial matrix were then incubated with RS for 24 h, and the permeability of the subendothelial matrix to DiI-LDL was measured.

Nuclear fractionation and extraction of proteins. Endothelial cells (HUVECs) were maintained in MCDB-131 medium with 0.5% FBS for at least 18 h, then stimulated with TNF-α (10 ng/mL) for 30 min with or without RS pretreatment for 24 h (100–500 μg/mL). Tissue homogenates of endothelial cells were resuspended in a buffer, which consisted of 10 mM HEPES (pH 7.8), 15 mM KCl, 2 mM MgCl2, 0.1 mM EDTA, 1 mM dithiotheitol (DTT), and 1 mM phenylmethylsulfonyl fluoride. After 10 min on ice, the tissue homogenates were pelleted and resuspended in two volumes of the buffer. Then, 3 M KCl was added dropwise to reach a 0.39 M KCl concentration. We extracted the nuclei from the cells with incubation for 1 h at 4 °C followed by centrifuged at 12,000*g* for 1 h. The supernatants were then dialyzed in a buffer, which consisted of 50 mM HEPES (pH 7.8), 50 mM KCl, 0.1 mM EDTA, 1 mM DTT, and 1 mM phenylmethylsulfonyl fluoride with 10% (v/v) glycerol. The samples were then cleared by centrifugation and stored at −80 °C until further use. Total protein concentration was determined by BCA (Thermo Fisher Scientific). We analyzed the levels and phosphorylation of IκBα, IKKα and IKKβ in cytosolic fractions by western blotting as described below. We measured p65 in the nuclear and cytosol fractions by Western blot studies. We used β-actin and Histone H3 as control for total protein in cytosolic or nuclear fractions. The activity of NF-κB in binding DNA was assessed in nuclear fractions by a DNA Binding TransAM NF-κBp65 Assay (Active Motif).

Western blotting. Cells (HUVECs) were lysed using RIPA lysis buffer with added protease and phosphatase inhibitors (10 μL/mL), EDTA (10 μL/mL) and phenylmethylsulfonyl fluoride (1 mM) (Thermo Fisher Scientific). They were sonicated for 3 min and then centrifuged at 10000*g* for 10 min to collect total protein fraction. Concentration was determined using the Pierce BCA Protein Assay (Thermo Fisher Scientific). We performed SDS PAGE on the samples using the Invitrogen NuPAGE Bis- Tris protein gels. The proteins were transferred to nitrocellulose membranes using the wet transfer method (BioRad). The membranes were blocked with 4% StartingBlock T20 Blocking Buffer (Thermo Fisher Scientific) with 0.1% Tween-20 in PBS or TBS for 1 h. The membranes were then incubated with the primary antibodies in 1% StartingBlock overnight at 4 °C (Supplemental Table 1). The membranes were then incubated with HP conjugated secondary antibodies (Cell Signaling) at 1:3500 dilution for 2 h in 1% Blotto. SuperSignal West Femto ECL solution (Thermo Fisher Scientific) was used to detect the antibodies and imaging was performed on a G:BOX imaging system (Syngene, Inc.).

Murine model of atherosclerosis. All animal studies were performed with the approval of the University of Texas at Austin Institutional Animal Care and Use Committee (IACUC) and in accordance with NIH guidelines "Guide for Care and Use of Laboratory Animals" for animal care. We used male and female $ApoE^{-/-}$ mice (B6·129P2-$Apoe^{tm1Unc}$/J) for this study (Jackson Laboratories, Inc.). The animals were given high fat chow which was the standard formulation Clinton/Cybulsky high fat rodent diet with regular casein and 1.25% added cholesterol (D12108C; Research Diets, Inc.). For RS treated animals, the high fat diet (HFD) was formulated with 0.75 g of RS per kg diet. At 12 weeks of age, the mice were switched from normal chow to high fat chow for 4 weeks. The HFD group remained on this diet for an additional 9 weeks while the treatment group was switched to high fat chow with RS. At 4, and 12 weeks after start of HFD, the vessels of the mice were imaged using high resolution ultrasound as described below. At 13 weeks of HFD, the mice were sacrificed, and the blood, heart, aorta, liver and white adipose tissues were harvested for further analysis. For control, we used male and female wild type mice (n = 5) fed a standard diet for 13 weeks. The mice were randomly assigned to the 3 groups and post-sacrificial analyses were performed in a blind manner.

High resolution ultrasound imaging. High resolution ultrasound was performed using the Visual Sonics VEVO 2100 system with the MS500D transducer in the $ApoE^{-/-}$ model. The mice were anesthetized with isoflurane and body temperature monitored using a probe. Prior to imaging, the fur on the chest was removed using Nair. First, the longitudinal section of the aortic arch was located using the B-mode option. Pulsed wave Doppler and 3D echocardiography images were then obtained for calculating peak systolic velocity (PSV), end diastolic velocity (EDV) and, mean velocity (MV). The longitudinal section of the left common carotid artery was located using B-mode and pulsed wave Doppler images were obtained for the same parameters in the carotid artery. Finally, the cross section of the aortic arch was imaged in B-mode and color Doppler. Diameter measurements of the aortic arch determined from cross sections were used to calculate circumferential strain using the following formula:

$$\frac{1}{2}\left(\left(\frac{Sys}{Dia}\right)^2 - 1\right) * 100$$

where sys and dia are the peak systolic and end diastolic diameters.

Histological staining. Aortic roots at optimal cutting temperature were embedded in NEG-50 and cut into 7 μm thick sections using a cryostat (CM1510 S; Leica). These sections were stained with Oil Red O/

hematoxylin to measure lipid depot using the protocol below. Individual lesion area was determined by averaging the maximal values. For the liver samples, the tissues were placed in NEG-50 embedding medium and then frozen in liquid nitrogen cooled isopentane. The samples were serially sectioned to create 7 μm thick cryosections and Oil Red-O staining was performed. The percentage of hepatocytes containing lipid droplets was determined for each 20 × magnification field. An average percentage of steatosis was then determined for the entire specimen. Images of sections of Oil Red-O were acquired using a microscope and their quantifications were performed using IP Win32 v4.5 software. In order to determine the degree of non-alcoholic fatty liver disease (NAFLD), H&E staining was performed on paraffin-embedded liver sections (4 μm thick) that were evaluated by a single-blinded clinical pathologist and the NAFLD Activity Score (NAS) was determined using the protocol below. For the fat tissues, white adipose tissues (gonadal and inguinal depots) were fixed overnight in 4% formaldehyde and paraffin sections were created using standard methods. The size of adipocytes in white adipose tissues were quantified in H&E staining using Image J software.

Oil Red-O staining. A stock Oil Red O (Electron Microscopy Sciences) solution was made with 3 mg/mL Oil Red O in 99% isopropanol. The stock was diluted in a 3:2 ratio in ultrapure water. Frozen cryosections were air dried and then fixed in 10% formalin. They were stained with Oil Red O and counterstained with Mayer's hematoxylin (Electron Microscopy Sciences). The sections were mounted with aqueous mounting medium for imaging (Vector Labs).

Immunostaining for tissues. Lesional macrophages (F4/80), vSMCs (α-SMA), PECAM-1, eNOS, IκBα and p-p65 were detected by immunoperoxidase or immunofluorescence (Supplemental Table 1). Positive staining was expressed as percentage of total plaque area or number of positive cells per lesion area. In each experiment, negative controls without the primary antibody or using a nonrelated antibody were included to check for nonspecific staining (Supplemental Fig. 1).

NAFLD activity score analysis. The NAS was calculated for each liver sample as described previously [33]. Briefly, the score is the sum of the scores for steatosis (0–3), lobular inflammation (0–3) and ballooning (0–2), with an overall range from 0 to 8. Steatosis score was also assessed to grade the percentage involvement by steatotic hepatocytes as follows: grade 0, 0–5%; grade 1, >5–33%; grade 2, >33–66%; grade 3, >66%. In addition, Brunt's histological scoring system was used to evaluate the degree of hepatocellular ballooning and lobular inflammation [34]. The degree of lobular inflammation was measured, numbering the inflammatory foci per 200 × field as follows: grade 0, no foci; grade 1, <2 foci; grade 2, 2–4 foci; grade 3, >4 foci. The degree of hepatocellular ballooning was assessed according to the presence of balloon hepatocytes as follows: grade 0, none; grade 1, few balloon cells; grade 2, many cells/prominent ballooning. Minimal criteria for steatohepatitis (NASH) included the combined presence of grade 1 steatosis, hepatocellular ballooning and lobular inflammation [33].

En face imaging of aorta. Atherosclerotic lesions were quantified by en face analysis of the whole aorta. For en face preparations, the aorta was opened longitudinally, from the heart to the iliac arteries, while still attached to the heart and major branching arteries in the body. The aorta from the heart to the iliac bifurcation was then removed and was pinned out on a white wax surface in a dissecting pan using stainless steel pins 0.2 mm in diameter. After overnight fixation with 4% paraformaldehyde and a rinse in PBS, the aortas were immersed for 6 min in a filtered solution containing 0.5% Oil Red-O, 35% ethanol and 50% acetone and destained in 80% ethanol. The Oil Red-O stained aortas were photographed, and the atherosclerotic lesions were quantified using IP Win32 v4.5 software.

Pharmacokinetics of rhamnan sulfate in vivo. To test for oral bioavailability of RS, male mice (C57BL/6; Jackson Labs) were given RS-FITC (0.25 g RS/kg mouse) though oral gavage. Mice were sacrificed at the time points of 0, 1, 4, 12 and 24 h (n = 2), and blood, aorta, liver and heart were harvested. The tissue samples were lysed and RS-FITC concentration measured by reading fluorescence intensity with correction for background fluorescence. A calibration curve was made for RS-FITC in each tissue to convert fluorescence to concentration.

To measure the half-life of RS in the blood a mouse was injected intravenously via the tail vein with 0.5 mg of FITC conjugated RS (FITC-RS). A 10 ml blood sample was collected from the saphenous vein 1 min after injection, and then every 5 min for 25 min. The blood samples were centrifuged at 12 000 rpm for 5 min and the plasma was used for fluorescence measurements. Fluorescence intensity was measured using a plate reader (BioTek). A calibration curve for FITC-RS in mouse plasma was created which allowed the conversion of fluorescence intensity into concentration. The plasma concentration data was fitted to an exponential (first order elimination process is assumed). Extrapolating from the resulting equation we estimate the concentration at t = 0 is 0.278 mg/mL. The apparent volume of distribution, V_D, is calculated from the relationship $V_D = \text{Dose}/C_p^0$, where C_p^0 is the concentration at t = 0. We calculated V_D to be 1.8 mL. This is approximately equal to the blood volume (the blood volume of a mouse is 77–80 mL/g). The half-life was calculated from the elimination rate constant ($t_{1/2} = \frac{\ln 2}{k}$). With the data above, ($k = 0.0328\ \text{min}^{-1}$) the half-life is 21.1 min. Extrapolating from the data, the concentration drops below the lowest effective concentration we have tested (1 mg/mL) after 170 min.

Raman spectroscopy. Raman imaging was performed using a custom built 830 nm confocal Raman microscope with a 60× water immersion objective (NA = 1.2; Olympus) [35]. The scattered light was collected by a spectrograph and a CCD camera though a 50 μm core diameter fiber, which also acts as the pinhole of the confocal system. Fresh sections with 10 μm thickness were mounted on low-background Raman substrates (magnesium fluoride window or quartz slide) for Raman imaging. For every animal, one liver section was prepared, and 2–5 regions of interest were randomly selected from each section. Raman imaging was performed with a 0.25 or 0.5 s integration time and a step size of 0.75 or 1 μm. Image size varied from 24 × 24 μm^2 to 40 × 40 μm^2. Data preprocessing was performed using MATLAB (R2017a, MathWorks). Preprocessing steps included wavenumber calibration, background removal, cosmic ray removal, smoothing, and fluorescence background removal. Spectra were normalized to the area under the curve between 600 and 1800 cm^{-1}. Cluster analysis was performed for each image by k-means algorithm [36]. The first 100 principal components accounting for 95%–99% of the variation in the data set served as the input for the k-means. Each image contained at most three clusters, annotated as the lipid-rich zone, protein-rich zone, and others. Only the spectra within the lipid-rich zone were extracted to calculate the degree of unsaturation. The average Raman spectrum of the lipid-rich zone was compared between different groups. The degree of unsaturation was calculated by the peak ratio of 1656 cm^{-1} (integrated from 1645 to 1675 cm^{-1}) to 1441 cm^{-1} (integrated from 1420 to 1480 cm^{-1}), which corresponds to the ratio of C═C stretching vibration and the band related to the CH_2 scissoring mode [36,37].

RNA sequencing and analysis. Liver tissue from mice was obtained through cryosectioning and RNA was isolated using the Qiagen RNeasy Mini Kit. RNA-seq was performed by Genewiz using an Illumina HiSeq 2500 sequencing machine. Briefly, mRNA library preparation was done by Poly(A) selection followed by 2x150 bp single index sequencing. Gene ontology was determined based on The Gene Ontology database.

Preparation of rhamnan sulfate and heparin biochip. Biotinylated RS or heparin was prepared by conjugating the reducing end to amine-PEG3-Biotin (Pierce) [38]. In brief, RS or heparin (2 mg) and amine-PEG3-Biotin (2 mg, Pierce) were dissolved in 200 μl H_2O and 10 mg $NaCNBH_3$ was added. The reaction mixture was heated at 70 °C for 24 h, after that a further 10 mg $NaCNBH_3$ was added and the reaction was heated at 70 °C for another 24 h. After cooling to room temperature, the mixture was desalted with the spin column (3000 MWCO). Biotinylated RS or heparin was collected, freeze-dried and used for surface plasmon resonance (SPR) chip preparation. The biotinylated RS or

heparin was immobilized to a streptavidin chip (GE Healthcare) based on the manufacturer's protocol. Successful immobilization of RS or heparin was confirmed by the observation of about 100 resonance unit (RU) increase on the sensor surface after 20 μl injection of RS or heparin (1 mg/mL). The control flow cell was prepared by 1 min injection with saturated biotin.

Surface plasmon resonance of binding between rhamnan sulfate and proteins. Recombinant human FGF-1 and FGF-2 were a gift from Amgen. We purchased human antithrombin III (AT) (Hyphen Biomed), recombinant human platelet-derived growth factor (PDGF-BB), NF-κB p50, and NF-κB p65 (Abcam). The interactions between RS and proteins were measured using the BIAcore 3000 SPR system (GE Healthcare). The protein samples were diluted in HBS-EP buffer (0.01 M HEPES, 0.15 M NaCl, 3 mM EDTA, 0.005% surfactant P20, pH 7.4). Different dilutions of protein samples were injected at a flow rate of 30 μL/min. At the end of the sample injection, HBS-EP buffer was flowed over the sensor surface to facilitate dissociation. After a 3 min dissociation time, 30 μL of 2 M NaCl was injected to fully regenerate the surface. The response was monitored as a function of time (sensorgram) at 25 °C.

Statistical analysis. All results are shown as mean ± standard error of the mean. Comparisons between only two groups were performed using a 2-tailed Student's t-test. Multiple comparisons between groups were analyzed by 2-way ANOVA followed by a Tukey post-hoc test. A 2-tailed probability value $p < 0.05$ was considered statistically significant.

3. Results

Rhamnan sulfate is internalized by macropinocytosis and is dependent on proliferation in vSMCs. To examine the kinetics of uptake of RS by vascular cells, we incubated endothelial cells and aortic vSMCs with FITC-labeled RS. We found that RS was detectable after 24 h and that there was nuclear fluorescence from the RS after 48 h (Fig. 1A). Based on the timing of the nuclear localization of RS, we hypothesized that RS was entering the nucleus during the disassembly and reassembly of the nuclear envelope during cell division. To test this hypothesis, we mitotically arrested cells using mitomycin and measured RS uptake. In vSMCs, mitomycin significantly inhibited the uptake and nuclear localization of RS (Fig. 1A and B). However, this effect was not seen in endothelial cells (Fig. 2C). We also treated the cells with inhibitors of caveolin-mediated endocytosis (nystatin) and clathrin-mediated endocytosis (Pitstop 2) but neither had clear inhibitory effects on RS uptake (Fig. 1D, E, 2D, 2E). In contrast, treatment with an inhibitor of macropinocytosis (rottlerin) significantly inhibited uptake of RS in both endothelial cells and vSMCs (Figs. 1C, 2A and 2B).

Rhamnan sulfate decreases proliferation and migration of vascular cells. The proliferation and migration of vSMCs in atherosclerosis and vascular injury is an important mechanism in the development of intimal hyperplasia and remodeling of atherosclerotic plaques [39]. Endothelial proliferation and migration can be beneficial in vascular healing and reendothelialization following endothelial denudation [40]. However, these processes are also important for plaque neovascularization, which may have a role in thromboembolism and plaque destabilization [41]. We treated endothelial cell and vSMCs with RS and assayed their proliferation and migration in response to growth factors. Treatment with RS significantly reduced proliferation and migration of endothelial cells treated with FGF-2 (Fig. 3A–C). In vSMCs, RS decreased proliferation and migration in response to PDGF-BB (Fig. 3D–F). We also found that RS binds with high affinity to FGF-2 ($K_D = 2.6 \times 10^{-8}$ M) and PDGF-BB ($K_D = 2.8 \times 10^{-8}$ M; Supplemental Fig. 2; Supplemental Table 2). Proliferation and migration decreased in vSMCs treated with RS and FGF-2 (Fig. 3G and H).

Rhamnan sulfate enhances endothelial barrier function. We next examined whether RS could alter endothelial barrier function to LDL in the presence of treatments that induce inflammation or simulate the destruction of the glycocalyx. We treated endothelial cells with heparinase III, a bacterial enzyme that degrades heparan sulfate. In untreated endothelial cells this led to a drop in heparan sulfate coverage of the cells from 96% to 36% of the cells (Fig. 4A and B). With RS treatment, this heparinase-induced reduction in coverage was reduced to 59%, indicating that RS prevented the degradation of endogenous heparan sulfate glycosaminoglycans (Fig. 4A and B). The permeability of the endothelium to LDL was lower in endothelial cells treated with RS, regardless of dose of heparinase applied (Fig. 4C). Using Transwell filters as the base, we also tested the effect of 30 min of RS incubation on the blank filter, subendothelial matrix and endothelial monolayer. Treatment with RS reduced LDL permeability by 2.7-fold for the blank filter, 8-fold for the subendothelial matrix and 4.4-fold for the endothelial monolayer (Fig. 4D). These results indicated that RS accumulates both in the matrix and on the endothelial monolayer, where it can provide enhanced barrier function. We also tested the effectiveness of RS in reducing LDL permeability in endothelial cells after combined treatment with TNF-α and the protein synthesis inhibitor cycloheximide (CHX). While LDL permeability increased after the TNF-α/CHX treatment in control cells, it remained at basal levels with RS incubation (Fig. 4E). In contrast we did not observe this effect with treatment with heparin (Fig. 4E). We also examined the permeability of endothelial monolayers to VLDL and found that it was lower with RS treatment (Fig. 4F). These results suggest that RS can reduce endothelial permeability to LDL and improve overall barrier function.

Rhamnan sulfate reduces TNF-α induced NF-κB activation in human endothelial cells. The NF-κB pathway is an important pathway in controlling endothelial inflammation and is implicated in atherosclerosis, lipid metabolism and control of vSMC proliferation [42,43]. In the canonical NF-κB pathway, an NF-κB dimer is sequestered in the cytoplasm though interaction with a member of the IκB family of proteins (eg. IκBα). Activation of a receptor leads to the recruitment of adaptor proteins followed by recruitment of the IκB kinase complex (IKK; typically consisting of IKKα, IKKβ and IKKγ), which subsequently phosphorylates IκB and eventually leads to its degradation. The destruction of IκB allows NF-κB dimers to translocate to the nucleus where they can control gene transcription. To examine if RS could alter signaling though the NF-κB pathway, we treated endothelial cells with TNF-α for varying times and measured the activation of NF-κB pathway signaling intermediates using western blotting. We found that TNF-α induced an increase in IκBα phosphorylation after 10 min of treatment, indicating activation of the NF-κB pathway and that treatment with RS reduced this response (Fig. 5A and B). After 30 min of TNF-α treatment there was increased IκBα degradation and this was not affected by RS but basal levels of IκBα were increased (Fig. 5C and D). We also found that NF-κBp65 protein levels significantly decreased by RS treatment in the nuclear fraction and increased in the cytoplasm fraction after 30 min of TNF-α treatment, indicating reduced activation of the NF-κB pathway (Fig. 5E and F; Supplemental Fig. 3). In addition, phosphorylation of IKK, the complex responsible for the phosphorylation of IκBα, was also significantly reduced by RS treatment (Fig. 5G and H). Together, these findings indicate that RS affects multiple steps in the canonical pathway of NF-κB activation by TNF-α. To further confirm these findings, we measured NF-κBp65 activity directly using a TransAM assay and found that activity was reduced in the nuclear extracts of TNF-α treated endothelial cells (Fig. 5I). As we had observed nuclear localization of RS in our trafficking studies, we hypothesized that RS may bind directly to some of the components of the NF-κB pathway. Using surface plasmon resonance, we found that RS binds with high affinity to NF-κBp50 ($K_D = 1.1 \times 10^{-7}$ M) and NF-κBp65 ($K_D = 2.3 \times 10^{-8}$ M; Fig. 5J and K). The dissociation constant for the proteins for binding to RS was comparable to binding with heparin (Supplemental Table 2).

Rhamnan sulfate has oral bioavailability and is found in vascular tissues after oral administration. Prior to conducting an *in vivo* experiment with oral RS, we studied the pharmacokinetics of the drug to calculate the clearance rate and uptake by aorta, heart, blood and liver. We introduced RS in mice though oral gavage and measured the concentration in tissues over 24 h. In the abdominal aorta, RS

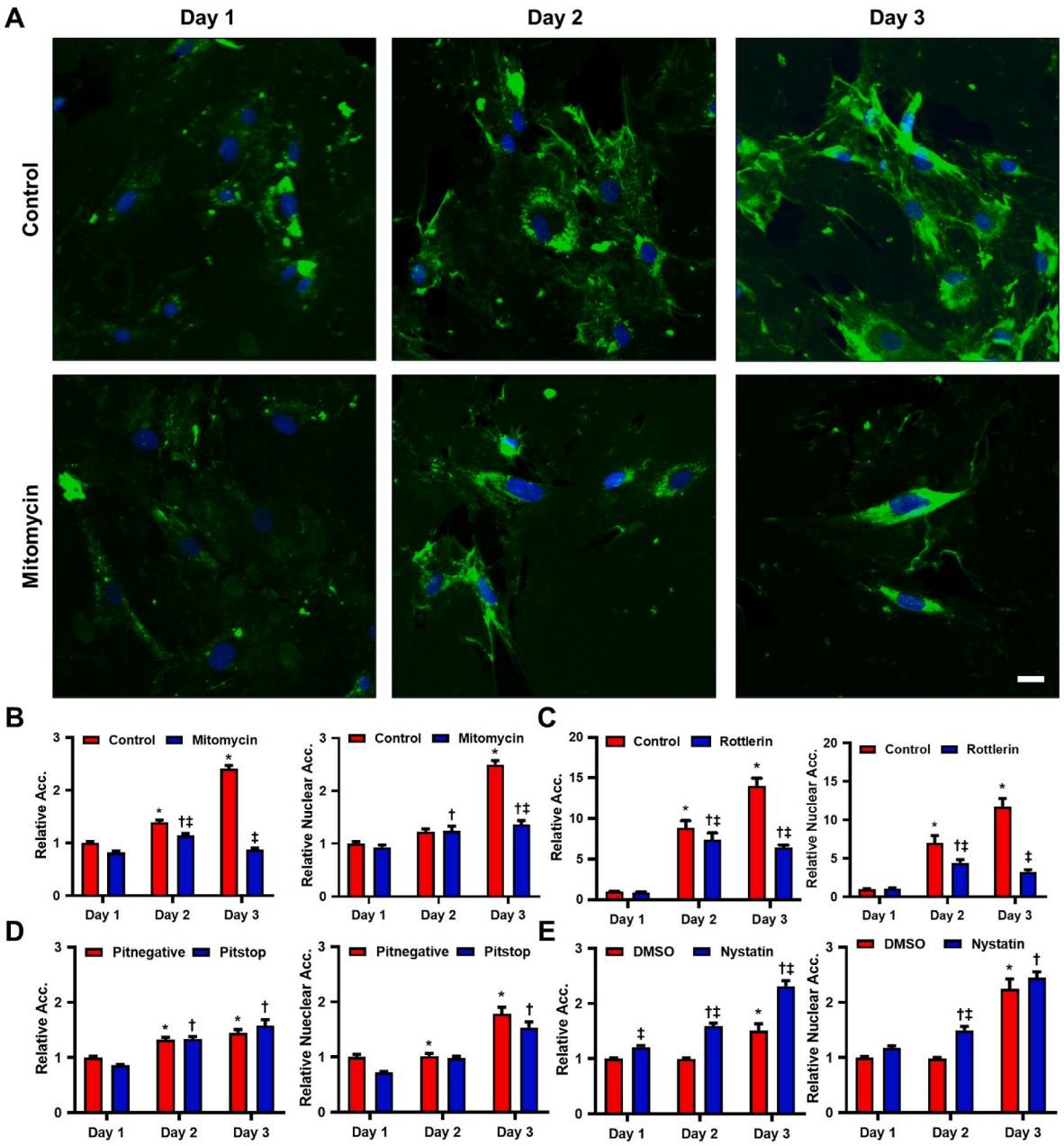

Fig. 1. Vascular smooth muscle cells internalize RS through mitosis and macropinocytosis. (A) Vascular smooth muscle cells were incubated with FITC-labeled RS (1000 μg/mL) with or without treatment with mitomycin, a mitosis inhibitor, for the indicated times. Scale bar = 20 μm. B) Uptake of RS in vSMCs treated with mitomycin decreased over three days (n = 10). For whole cell, $^{*}p < 0.0001$ control day 1 vs control day 2, $^{*}p < 0.0001$ control day 1 vs control day 3, $^{\dagger}p = 0.0014$ mitomycin day 1 vs mitomycin day 2, $^{\ddagger}p = 0.0117$ control day 2 vs mitomycin day 2, $^{\ddagger}p < 0.0001$ control day 3 vs mitomycin day 3. For nucleus, $^{*}p = 0.0096$ control day 1 vs control day 2, $^{*}p < 0.0001$ control day 1 vs control day 3, $^{\dagger}p = 0.0212$ mitomycin day 1 vs mitomycin day 3, $^{\ddagger}p < 0.0001$ control day 3 vs mitomycin day 3. (C) Treatment with rottlerin, an inhibitor of macropinocytosis, decreased RS accumulation (n = 10). For whole cell, $^{*}p < 0.0001$ control day 1 vs control day 2, $^{*}p < 0.0001$ control day 1 vs control day 3, $^{\dagger}p < 0.0001$ rottlerin day 1 vs rottlerin day 2, $^{\dagger}p < 0.0001$ rottlerin day 1 vs rottlerin day 3, $^{\ddagger}p < 0.0001$ control day 2 vs rottlerin day 2, $^{\ddagger}p < 0.0001$ control day 3 vs rottlerin day 3. For nucleus, $^{*}p < 0.0001$ control day 1 vs control day 2, $^{*}p < 0.0001$ control day 1 vs control day 3, $^{\dagger}p < 0.0001$ rottlerin day 1 vs rottlerin day 2, $^{\ddagger}p < 0.0001$ control day 2 vs rottlerin day 2, $^{\ddagger}p < 0.0001$ control day 3 vs rottlerin day 3. (D) No significant difference in uptake of RS on each day between control and vSMCs treated with pitstop 2, an inhibitor of clathrin-mediated endocytosis (n = 10). For whole cell, $^{*}p = 0.0259$ control day 1 vs control day 2, $^{*}p = 0.0029$ control day 1 vs control day 3, $^{\dagger}p < 0.0001$ pitstop day 1 vs pitstop day 2, $^{\dagger}p < 0.0001$ pitstop day 1 vs pitstop day 3. For nucleus, $^{*}p < 0.0001$ control day 1 vs control day 3, $^{\dagger}p = 0.0273$ pitstop day 1 vs pitstop day 2, $^{\dagger}p < 0.0001$ pitstop day 1 vs pitstop day 3. (E) Treatment with nystatin, an inhibitor of caveolin-mediated endocytosis, increased uptake (n = 10). For whole cell, $^{*}p < 0.0001$ control day 1 vs control day 3, $^{\dagger}p < 0.0001$ nystatin day 1 vs nystatin day 2, $^{\dagger}p < 0.0001$ nystatin day 1 vs nystatin day 3, $^{\ddagger}p = 0.0407$ control day 1 vs nystatin day 1, $^{\ddagger}p < 0.0001$ control day 2 vs nystatin day 2, $^{\ddagger}p < 0.0001$ control day 3 vs nystatin day 3. For nucleus, $^{*}p < 0.0001$ control day 1 vs control day 3, $^{\dagger}p < 0.0001$ nystatin day 1 vs nystatin day 2, $^{\dagger}p < 0.0001$ nystatin day 1 vs nystatin day 3, $^{\ddagger}p < 0.0001$ control day 2 vs nystatin day 2.

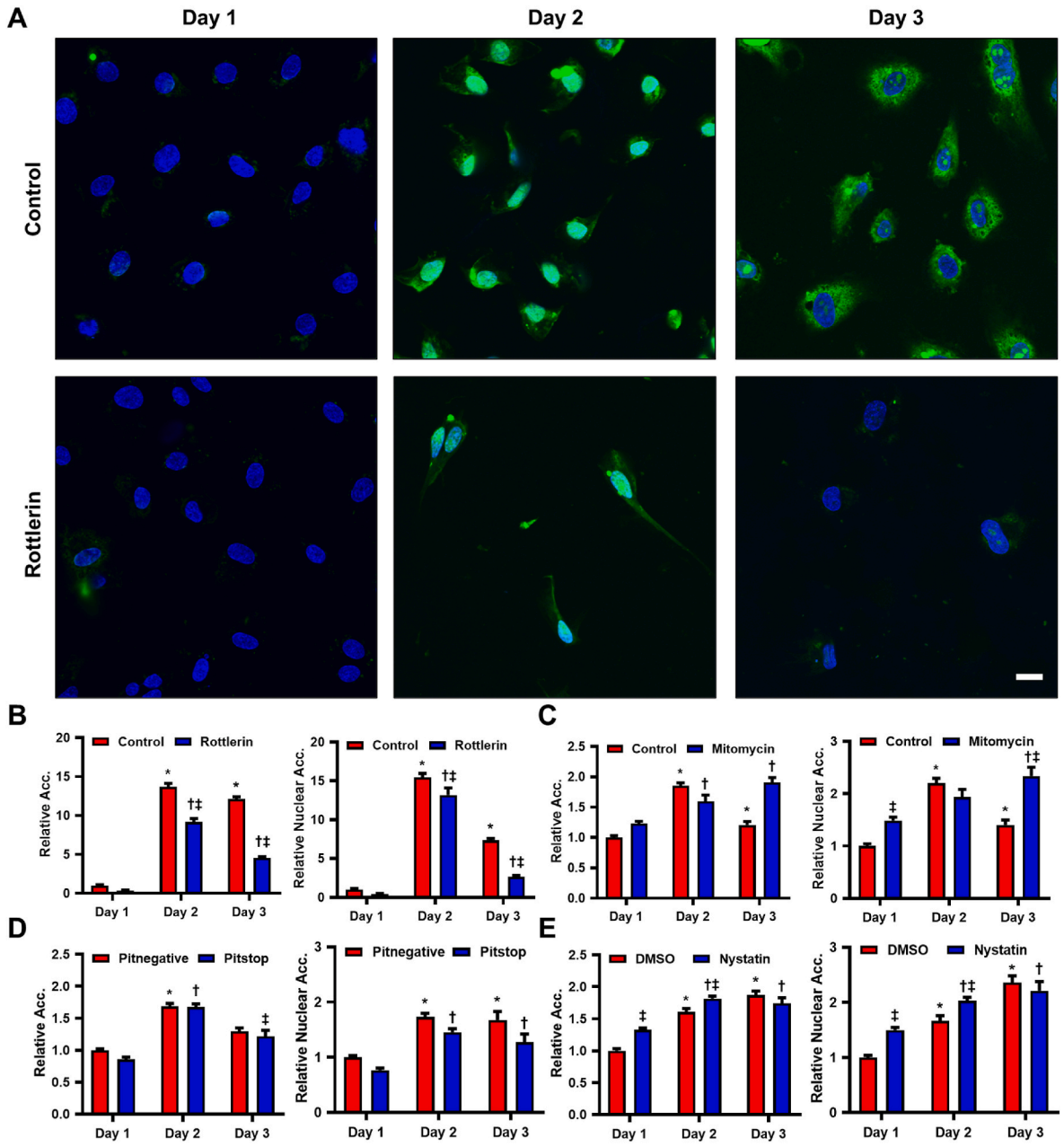

Fig. 2. Endothelial cells internalize RS primarily through macropinocytosis. (A) Endothelial cells were incubated with FITC-labeled RS (1000 μg/mL) with or without treatment with rottlerin. Scale bar = 20 μm. B) In endothelial cells treated with rottlerin, uptake of RS was lower compared to control (n = 10). For whole cell, $^{*}p < 0.0001$ control day 1 vs control day 2, $^{*}p < 0.0001$ control day 1 vs control day 3, $^{\dagger}p < 0.0001$ rottlerin day 1 vs rottlerin day 2, $^{\dagger}p < 0.0001$ rottlerin day 1 vs rottlerin day 3, $^{\ddagger}p < 0.0001$ control day 2 vs rottlerin day 2, $^{\ddagger}p < 0.0001$ control day 3 vs rottlerin day 3. For nucleus, $^{*}p < 0.0001$ control day 1 vs control day 2, $^{*}p < 0.0001$ control day 1 vs control day 3, $^{\dagger}p < 0.0001$ rottlerin day 1 vs rottlerin day 2, $^{\dagger}p < 0.0001$ rottlerin day 1 vs rottlerin day 3, $^{\ddagger}p = 0.0004$ control day 2 vs rottlerin day 2, $^{\ddagger}p < 0.0001$ control day 3 vs rottlerin day 3. (C) In endothelial cells treated with mitomycin, uptake of RS appeared to increase over three days compared to control (n = 10). For whole cell, $^{*}p < 0.0001$ control day 1 vs control day 2, $^{*}p < 0.0001$ control day 1 vs control day 3, $^{\dagger}p = 0.0313$ mitomycin day 1 vs mitomycin day 2, $^{\dagger}p = 0.0313$ mitomycin day 1 vs mitomycin day 3. For nucleus, $^{*}p < 0.0001$ control day 1 vs control day 2, $^{*}p = 0.0089$ control day 1 vs control day 3, $^{\dagger}p = 0.0008$ mitomycin day 1 vs mitomycin day 3, $^{\ddagger}p = 0.0001$ control day 1 vs mitomycin day 1, $^{\ddagger}p < 0.0001$ control day 3 vs mitomycin day 3. (D) Some reduction in RS uptake on day 3 in control and cells treated with pitstop 2 (n = 10). For whole cell, $^{*}p < 0.0001$ control day 1 vs control day 2, $^{\dagger}p < 0.0001$ pitstop day 1 vs pitstop day 2, $^{\ddagger}p = 0.0042$ control day 3 vs pitstop day 3. For nucleus, $^{*}p < 0.0001$ control day 1 vs control day 2, $^{*}p < 0.0001$ control day 1 vs control day 3, $^{\dagger}p = 0.0313$ pitstop day 1 vs pitstop day 2, $^{\dagger}p = 0.0313$ pitstop day 1 vs pitstop day 3. (E) Treatment with nystatin increased uptake of RS compared to control on day 2 of incubation (n = 10). For whole cell, $^{*}p < 0.0001$ control day 1 vs control day 2, $^{*}p < 0.0001$ control day 1 vs control day 3, $^{\dagger}p < 0.0001$ nystatin day 1 vs nystatin day 2, $^{\dagger}p < 0.0001$ nystatin day 1 vs nystatin day 3, $^{\ddagger}p = 0.0003$ control day 1 vs nystatin day 1, $^{\ddagger}p = 0.0002$ control day 2 vs nystatin day 2. For nucleus, $^{*}p < 0.0001$ control day 1 vs control day 2, $^{*}p < 0.0001$ control day 1 vs control day 3, $^{\dagger}p < 0.0001$ nystatin day 1 vs nystatin day 2, $^{\dagger}p < 0.0001$ nystatin day 1 vs nystatin day 3, $^{\ddagger}p = 0.0033$ control day 1 vs nystatin day 1, $^{\ddagger}p = 0.0034$ control day 2 vs nystatin day 2.

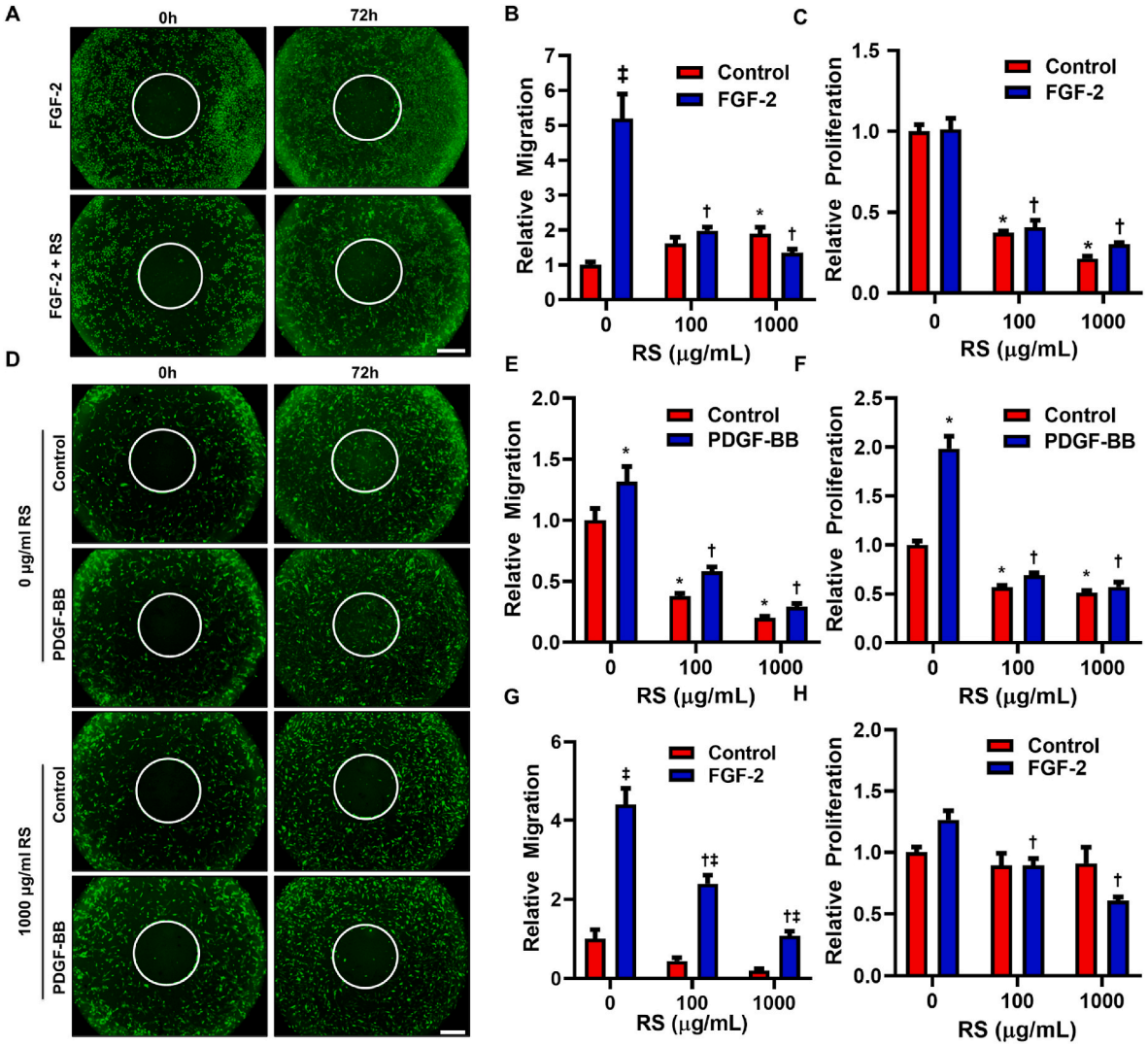

Fig. 3. Rhamnan sulfate decreases proliferation and migration of vascular cells. (A) Endothelial cells were treated with FGF-2 and RS in ORIS assay. Scale bar = 100 μm. (B) Migration of endothelial cells treated with FGF-2 was reduced by RS (n = 10). *$p = 0.0083$ 0 μg/mL RS vs 1000 μg/mL RS, †$p = 0.0166$ 0 μg/mL RS + FGF-2 vs 100 μg/mL RS + FGF-2, †$p = 0.0051$ 0 μg/mL RS + FGF-2 vs 1000 μg/mL RS + FGF-2, ‡$p = 0.0027$ 0 μg/mL RS vs 0 μg/mL RS + FGF-2. (C) Proliferation of endothelial cells treated with FGF-2 and RS decreased after 72 h (n = 16). *$p < 0.0001$ 0 μg/mL RS vs 100 μg/mL RS, *$p < 0.0001$ 0 μg/mL RS vs 1000 μg/mL RS, †$p < 0.0001$ 0 μg/mL RS + FGF-2 vs 100 μg/mL RS + FGF-2, †$p < 0.0001$ 0 μg/mL RS + FGF-2 vs 1000 μg/mL RS + FGF-2. (D) Vascular smooth muscle cells expressing GFP were treated with PDGF-BB and 0, 100 and 1000 μg/mL of RS in ORIS assay. Scale bar = 100 μm. (E) Migration of vSMCs treated with PDGF-BB was decreased by RS (n = 10). *$p < 0.0001$ 0 μg/mL RS vs 100 μg/mL RS, *$p < 0.0001$ 0 μg/mL RS vs 1000 μg/mL RS, †$p < 0.0001$ 0 μg/mL RS + PDGF-BB vs 100 μg/mL RS + PDGF-BB, †$p < 0.0001$ 0 μg/mL RS + PDGF-BB vs 1000 μg/mL RS + PDGF-BB, ‡$p = 0.0259$ 0 μg/mL RS vs 0 μg/mL RS + PDGF-BB. (F) Vascular smooth muscle cells treated with PDGF-BB and RS proliferated less after 72 h (n = 16). *$p < 0.0001$ 0 μg/mL RS vs 100 μg/mL RS, *$p < 0.0001$ 0 μg/mL RS vs 1000 μg/mL RS, †$p < 0.0001$ 0 μg/mL RS + PDGF-BB vs 100 μg/mL RS PDGF-BB, †$p < 0.0001$ 0 μg/mL RS + PDGF-BB vs 1000 μg/mL RS + PDGF-BB, ‡$p < 0.0001$ 0 μg/mL RS vs 0 μg/mL RS + PDGF-BB. (G) Migration of cells vSMCs treated with FGF-2 and RS increased after 72 h of treatment (n = 10). †$p < 0.0001$ 0 μg/mL RS + FGF-2 vs 100 μg/mL RS + FGF-2, †$p < 0.0001$ 0 μg/mL RS + FGF-2 vs 1000 μg/mL RS + FGF-2, ‡$p < 0.0001$ 0 μg/mL RS vs 0 μg/mL RS + FGF-2, ‡$p < 0.0001$ 100 μg/mL RS vs 100 μg/mL RS + FGF-2, ‡$p = 0.0458$ 1000 μg/mL RS vs 1000 μg/mL RS + FGF-2. (H) Proliferation of vSMCs induced by FGF-2, was also reduced after 72 h with RS treatment (n = 16). †$p = 0.0033$ 0 μg/mL RS + FGF-2 vs 100 μg/mL RS + FGF-2, †$p < 0.0001$ 0 μg/mL RS + FGF-2 vs 1000 μg/mL RS + FGF-2.

concentration started decreasing after 4 h but continued to rise steadily for 24 h in the thoracic aorta (Supplemental Fig. 4A). In the heart and total blood plasma, RS concentrations increased up to 4 and 12 h respectively before being cleared (Supplemental Fig. 4B). In the liver, there was an initial influx of RS at 4 h and then a gradual increase in concentration after 12 h (Supplemental Fig. 4B). We also injected FITC labeled RS into the blood directly and examined its clearance. We calculated the half-life of RS to be approximately 21.1 min in the blood following intravenous injection (Supplemental Fig. 4C).

Orally administered rhamnan sulfate decreases plaque deposition in ApoE$^{-/-}$ mice on a high fat diet. To test the effect of RS on the progression of atherosclerosis, ApoE$^{-/-}$ mice were fed a high fat diet or a high fat diet supplemented with RS for 13 weeks (Supplemental Fig. 5). Blood cholesterol levels were decreased significantly in female ApoE$^{-/-}$ mice treated with RS but not in male mice (Fig. 6A). There was no change in plasma triglyceride levels in both male and female mice (Supplemental Fig. 6A). We measured ox-LDL and TNF-α levels in plasma (Supplemental Figs. 6B and C). There was no statistical significance for ox-LDL levels in the RS treated groups. In female mice, TNF-α was lower in RS treated group compared to the HFD group, while in male mice it was higher. In en face preparations of the aorta, lipid deposition was decreased by 45.2% in female and 36.4% in male mice whole aortas with RS treatment in comparison to the ApoE$^{-/-}$ HFD group (Fig. 6B and C). In the aortic arch, there was also significant

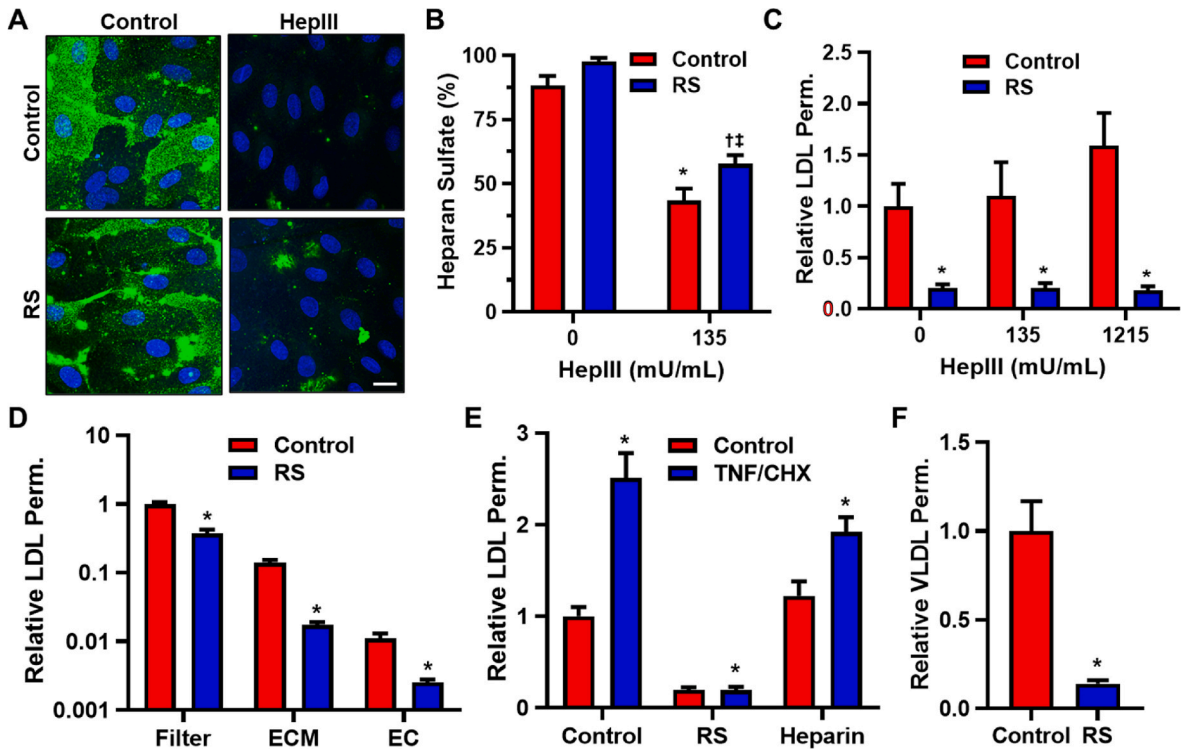

Fig. 4. Rhamnan sulfate reduces LDL permeability in endothelial cells. (A) Endothelial cells were treated with RS (25 μg/mL) and heparinase III (135 mU/mL) and immunostained for heparan sulfate. Scale bar = 20 μm. (B) Heparan sulfate coverage, reduced by heparinase III, was increased in ECs treated with RS (n = 8). *$p <$ 0.0001 0 mU/mL heparinase III vs 135 mU/mL heparinase III, †$p <$ 0.0001 0 mU/mL heparinase III + RS vs 135 mU/mL heparinase III + RS, ‡$p = 0.0308$ 135 mU/mL heparinase III vs 135 mU/mL heparinase III + RS. (C) Permeability of LDL was decreased in ECs treated with RS regardless of heparinase III dose (n = 4–8). *$p =$ 0.0012 0 mU/mL heparinase III vs RS, *$p = 0.0012$ 135 mU/mL heparinase III vs 135 mU/mL heparinase III + RS, *$p <$ 0.0001 1215 mU/mL heparinase III vs 1215 mU/mL heparinase III + RS. (D) Permeability of LDL was reduced in blank Transwell filters and those with subendothelial matrix and endothelial cell monolayer with RS incubation (n = 4). *$p = 0.0003$ control vs RS for filter, *$p <$ 0.0001 control vs RS for ECM, *$p = 0.0066$ control vs RS for cells. (E) Permeability of LDL was lower with RS treatment despite addition of TNF-α and cycloheximide. Heparin treatment produced no change in the same conditions (n = 4–19). *$p <$ 0.0001 control vs TNF-α/chx, *$p <$ 0.0001 RS vs RS + TNF-α/chx, *$p = 0.0116$ heparin vs heparin + TNF-α/chx. (F) Permeability of VLDL also decreased by RS treatment (n = 8). *$p <$ 0.0001 control vs RS.

decrease in lipid deposition in the male and female ApoE$^{-/-}$ mice with RS treatment. Stenosis decreased in female mice only (Fig. 6D and E). In the thoracic aorta, there was a reduction in lipid deposition, lesion area and stenosis for female mice treated with RS but not for male mice (Fig. 6F and G).

Oral rhamnan sulfate does not affect body weight or adipose tissue deposition in ApoE$^{-/-}$ mice. There was no difference in the weight of the mice between the RS treated and untreated mice for both male and female groups (Supplemental Figs. 7A and B). There was also no significant difference in the ratio of liver, inguinal white adipose tissue (iWAT) and gonadal white adipose tissue (gWAT) to total body weight in female mice (Supplemental Fig. 7C) but there was a significant increase in gWAT in male mice but not in liver or iWAT (Supplemental Fig. 7D). Also, characterization of the iWAT and gWAT showed no change in size of adipocytes in treated female mice (Supplemental Fig. 8A). The size of adipocytes remained the same in both iWAT and gWAT in the HFD and HFD + RS treated groups (Supplemental Fig. 8B).

Rhamnan sulfate treatment reduces high fat diet induced increases in blood velocity in ApoE$^{-/-}$ mice. To monitor plaque development over the course of the experiment, we measured blood velocity in the aorta and left common carotid arteries of ApoE$^{-/-}$ mice. Peak systolic velocity (PSV), end diastolic velocity (EDV) and mean velocity (MV) were calculated in the ascending and descending aorta, aortic arch and, carotid artery. In female mice, PSV, EDV and, MV decreased with RS treatment in the ascending aorta (Supplemental Fig. 9; Supplemental Fig. 10A). In the aortic arch for female mice, there was no change in blood flow velocities with RS treatment but there was a significant decrease in flow velocities in the descending aorta for the PSV and EDV with RS treatment (Supplemental Fig. 9). All flow velocities decreased in the carotid artery with RS treatment as well for female mice (Supplemental Fig. 9; Supplemental Fig. 11A). In male mice, there was no change in all three velocities in the ascending aorta and aortic arch with RS treatment (Supplemental Fig. 9; Supplemental Fig. 10B). In the descending aorta, PSV, EDV and, MV all decreased with RS treatment while there no change in the velocities in the carotid artery (Supplemental Fig. 9; Supplemental Fig. 11B). In addition, we found that the elasticity, measured by circumferential strain, of the aorta during the cardiac cycle was higher in female mice treated with RS (Supplemental Fig. 12).

Rhamnan sulfate reduces vascular inflammation in female mice but not male mice. To quantify the efficacy of oral RS in reducing vascular inflammation, we examined the presence of macrophages and activation of the NF-κB pathway in the ApoE$^{-/-}$ mice treated with HFD or HFD with RS supplementation. There was a significant decrease in macrophages (F4/80 positive cells) in histological sections from the aortic root in female mice treated with RS in comparison to the HFD group but there was no change in male mice (Fig. 7A and B). Also, IκBα, an inhibitor of NF-κB, was significantly upregulated in female mice (Fig. 7C and D). Phosphorylation of the p65 subunit of NF-κB was also reduced in female ApoE$^{-/-}$ mice on a HFD treated with RS (Fig. 7E; Supplemental Fig. 13). Phosphorylation of p65, IκBα and F4/80 were not affected by RS treatment in male mice (Fig. 7B, D, E).

Treatment with RS reduces plaque angiogenesis and enhances endothelial eNOS production in ApoE$^{-/-}$ mice on a high fat diet. During atherosclerotic inflammation, endothelial permeability is increased by PECAM-1 upregulation as it promotes leukocyte

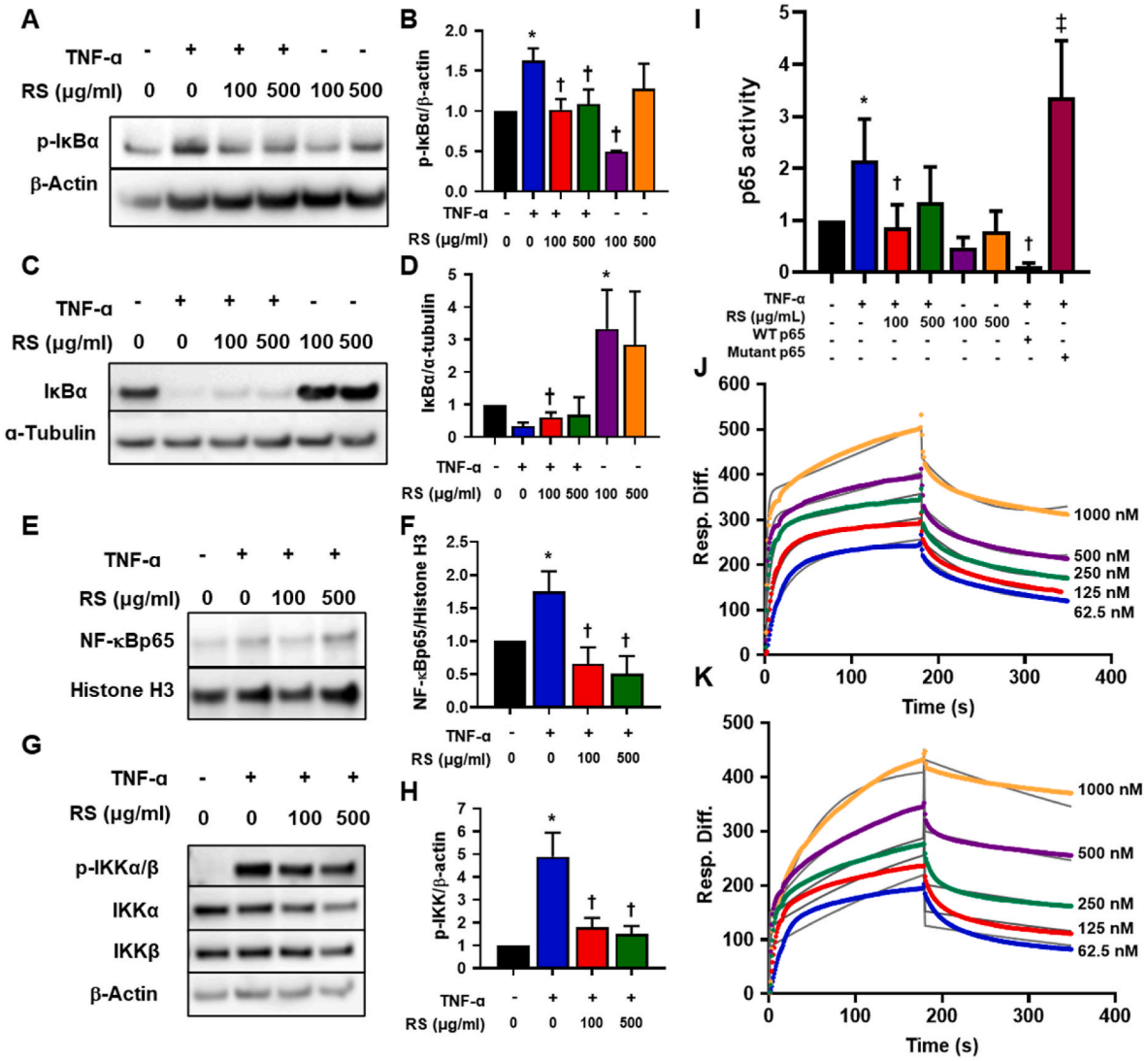

Fig. 5. Rhamnan sulfate reduces NF-κB activation in endothelial cells. (A) Endothelial cells were treated with TNF-α (10 ng/mL) for 10 min to cause IκBα phosphorylation. (B) Western blot analysis showed decrease in p-IκBα in total protein of cells pre-treated with RS (n = 2–15). *$p = 0.0025$ control vs TNF-α, †$p = 0.0172$ TNF-α vs TNF-α+100 μg/mL RS, †$p = 0.0153$ TNF-α vs TNF-α+500 μg/mL RS, †$p = 0.0044$ TNF-α vs 100 μg/mL RS. (C) Endothelial cells were treated with TNF-α (10 ng/mL) for 30 min to cause degradation of IκBα phosphorylation. (D) Western blotting showed increase in IκBα in the absence of TNF-α with RS treatment (n = 7–11). *$p < 0.0241$ control vs 100 μg/mL RS, †$p = 0.0125$ TNF-α+100 μg/mL RS vs 100 μg/mL RS. (E) Endothelial cells were treated with TNF-α (10 ng/mL) for 30 min to cause NF-κB translocation into the nucleus. (F) Western blotting showed decrease in p65 subunit of NF-κB in nuclear fraction of cells pre-treated with RS (n = 6). *$p = 0.0403$ control vs TNF-α, †$p = 0.0098$ TNF-α vs TNF-α+100 μg/mL RS, †$p = 0.0069$ TNF-α vs TNF-α+500 μg/mL RS. (G) Endothelial cells were treated with TNF-α (10 ng/mL) for 10 min to cause activation of the IKK complexes. (H) Western blotting showed decrease in p-IKKα/β but no change in IKKα and IKKβ in total protein of cells pre-treated with RS (n = 2–11). *$p < 0.0001$ control vs TNF-α, †$p = 0.0048$ TNF-α vs TNF-α+100 μg/mL RS, †$p = 0.0018$ TNF-α vs TNF-α+500 μg/mL RS. (I) TransAM assay showed reduced NF-κB/p65 activity after treatment with 100 μg/mL RS dose (n = 8). *$p = 0.0174$ control vs TNF-α, †$p = 0.0057$ TNF-α vs TNF-α+100 μg/mL RS, †$p = 0.0067$ TNF-α vs WT p65, ‡$p = 0.0236$ WT p65 vs mutant p65. Dilutions of (J) NF-κB/p65 and (K) NF-κB/p50 were introduced on a sensor surface with RS and dissociation with HBS-EP buffer measured for 3 min. After 3 min, the surface was regenerated with 2 M NaCl and total response monitored in sensorgram (n = 5).

transmigration and integrin activation. In both female and male ApoE$^{-/-}$ mice, PECAM-1 was decreased with RS treatment (Fig. 7F; Supplemental Fig. 13). Impaired eNOS levels lead to atherogenesis though increased nitric oxide breakdown and superoxide production [44]. In female mice treated with RS, there was higher eNOS production in the aortic arch (Fig. 7G; Supplemental Fig. 13). There was increased area of α-SMA staining in the aortic arch of female ApoE$^{-/-}$ mice treated with RS, reflecting the reduction in plaque size (Fig. 7H; Supplemental Fig. 13). In male mice, eNOS and α-SMA were not affected by RS treatment (Fig. 7G and H). In addition, we evaluated elastic lamina degradation in the histological section and found that there was decreased elastic lamina degradation in the RS treated mice of both sexes (Supplemental Fig. 14).

Hepatic steatosis is decreased by oral RS treatment *in vivo*. Non-alcoholic fatty liver disease (NAFLD) has been correlated with the development of atherosclerosis and is linked to inflammation, metabolic syndrome and obesity [45,46]. To test the effect of RS on hepatic lipid deposition, we performed histological analysis and Raman spectroscopy on tissue sections from ApoE$^{-/-}$ mice. We quantified NAS scores (a sum of histopathological scores for steatosis, inflammation and ballooning) for the livers from the mice treated with HFD or HFD + RS. In female mice, NAS scores reduced with RS treatment but appeared to increase in male mice (Fig. 8A and B). There was also a marked reduction in lipid deposition in the livers of female mice but no change in lipid deposition for male mice treated with RS (Fig. 8C and D). Analysis of the livers with Raman spectroscopy indicated that the lipids in male mice livers were

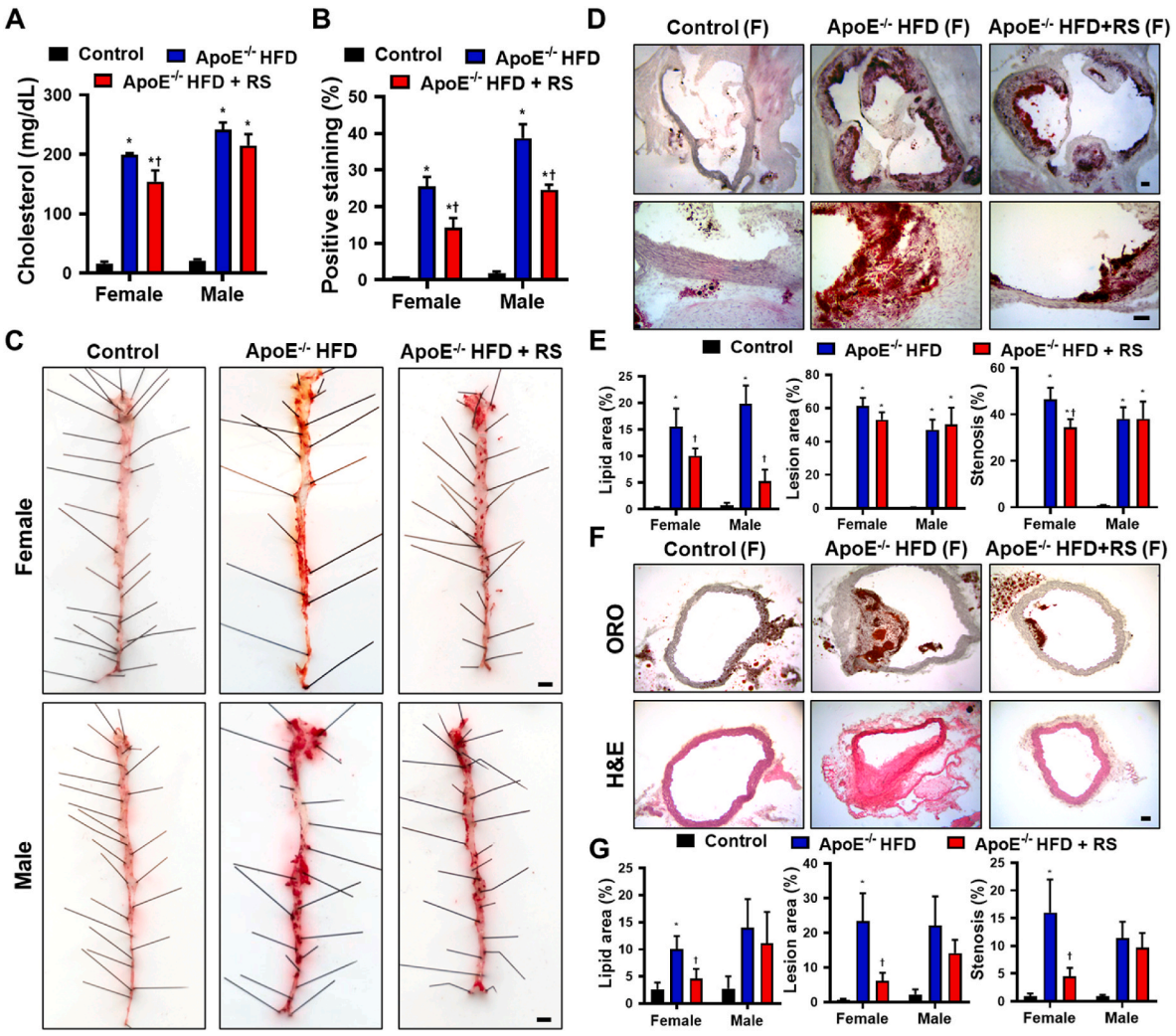

Fig. 6. Rhamnan sulfate reduces atherosclerotic plaque area and plasma cholesterol in ApoE$^{-/-}$ mice. (A) Plasma cholesterol was lower by 22.5% in female ApoE$^{-/-}$ mice fed HFD and RS (n = 10). For female mice, $^{*}p < 0.0001$ control vs ApoE$^{-/-}$ HFD, $^{*}p < 0.0001$ control vs ApoE$^{-/-}$ HFD + RS, $^{\dagger}p = 0.0420$ ApoE$^{-/-}$ HFD vs ApoE$^{-/-}$ HFD + RS. For male mice, $^{*}p < 0.0001$ control vs ApoE$^{-/-}$ HFD, $^{*}p < 0.0001$ control vs ApoE$^{-/-}$ HFD + RS. (B) Lipid deposition in the whole aorta was reduced by 45.2% in female and 36.4% in male ApoE$^{-/-}$ mice fed HFD and RS (n = 3). For female mice, $^{*}p = 0.0028$ control vs ApoE$^{-/-}$ HFD, $^{*}p = 0.0362$ control vs ApoE$^{-/-}$ HFD + RS, $^{\dagger}p = 0.0429$ ApoE$^{-/-}$ HFD vs ApoE$^{-/-}$ HFD + RS. For male mice, $^{*}p = 0.0006$ control vs ApoE$^{-/-}$ HFD, $^{*}p = 0.0057$ control vs ApoE$^{-/-}$ HFD + RS, $^{\dagger}p = 0.0262$ ApoE$^{-/-}$ HFD vs ApoE$^{-/-}$ HFD + RS. (C) En face staining of aortas of female and male mice for C57BL/6 mice fed a standard diet, ApoE$^{-/-}$ mice fed a HFD and ApoE$^{-/-}$ mice fed a HFD with RS. Scale bar = 100 μm. (D) Aortic arch sections of female (shown) and male mice in the three groups were stained with Oil Red-O. Scale bar = 100 μm. (E) Lipid deposition, lesion area and stenosis were reduced in aortic arches of female ApoE$^{-/-}$ mice fed HFD with RS. Lipid deposition only was reduced in aortic arches of male ApoE$^{-/-}$ mice fed HFD with RS (n = 7). For lipid area, $^{*}p = 0.0028$ female control vs ApoE$^{-/-}$ HFD, $^{\dagger}p = 0.0462$ female ApoE$^{-/-}$ HFD vs ApoE$^{-/-}$ HFD + RS, $^{*}p = 0.0036$ male control vs ApoE$^{-/-}$ HFD, $^{\dagger}p = 0.0043$ male ApoE$^{-/-}$ HFD vs ApoE$^{-/-}$ HFD + RS. For lesion area, $^{*}p < 0.0001$ female control vs ApoE$^{-/-}$ HFD, $^{*}p < 0.0001$ female control vs ApoE$^{-/-}$ HFD, $^{*}p = 0.0029$ male control vs ApoE$^{-/-}$ HFD, $^{*}p = 0.0021$ male control vs ApoE$^{-/-}$ HFD. For stenosis, $^{*}p < 0.0001$ female control vs ApoE$^{-/-}$ HFD, $^{*}p < 0.0001$ female control vs ApoE$^{-/-}$ HFD + RS, $^{\dagger}p = 0.0082$ female ApoE$^{-/-}$ HFD vs ApoE$^{-/-}$ HFD + RS, $^{*}p = 0.0021$ male control vs ApoE$^{-/-}$ HFD, $^{*}p = 0.0026$ male control vs ApoE$^{-/-}$ HFD. (F) Histological sections of the thoracic aorta of female (shown) and male mice in the three groups were stained with Oil Red-O and hematoxylin and eosin. Scale bar = 100 μm. (G) Lipid deposition, lesion area and stenosis were reduced in thoracic aortas of female ApoE$^{-/-}$ mice fed a HFD with RS (n = 7). For lipid area, $^{*}p = 0.0074$ female control vs ApoE$^{-/-}$ HFD, $^{\dagger}p = 0.0207$ female ApoE$^{-/-}$ HFD vs ApoE$^{-/-}$ HFD + RS. For lesion area, $^{*}p = 0.0209$ female control vs ApoE$^{-/-}$ HFD, $^{\dagger}p = 0.0405$ female ApoE$^{-/-}$ HFD vs ApoE$^{-/-}$ HFD + RS. For stenosis, $^{*}p = 0.0102$ female control vs ApoE$^{-/-}$ HFD, $^{\dagger}p = 0.0173$ female ApoE$^{-/-}$ HFD vs ApoE$^{-/-}$ HFD + RS. (For interpretation of the references to color in this figure legend, the reader is referred to the Web version of this article.)

less saturated in the RS treated group in comparison to the HFD group (Fig. 8*E*–G). In addition, the overall size of lipid droplets decreased in both male and female livers after RS treatment (Fig. 8E).

Expression of lipid metabolism, liver inflammation and circadian rhythm genes in the liver are altered by RS treatment. To further understand the sex-specific differences in the response to RS, we performed a transcriptomic analysis on the livers from the ApoE mice used in the atherosclerosis study. A differential gene expression analysis revealed that RS treatment that there were only a limited number of genes that were significantly regulated by RS in the female mice but a much larger number of genes regulated by RS in the male mice (Fig. 9A and B; Supplemental Fig. 15). There were some genes in common in both male and female mice with RS but there was a large set of genes that were differentially regulated between the groups (Fig. 9B–D; Supplemental Fig. 16). A gene ontology analysis showed that male mice treated with RS, there were changes in pathways circadian rhythm and lipid metabolism (Supplemental Fig. 17A). A similar analysis in female mice demonstrated significant alterations in pathways relating to lipid and drug metabolism (Supplemental Fig. 17B). An analysis of the individual genes that were regulated in common between the male and female mice

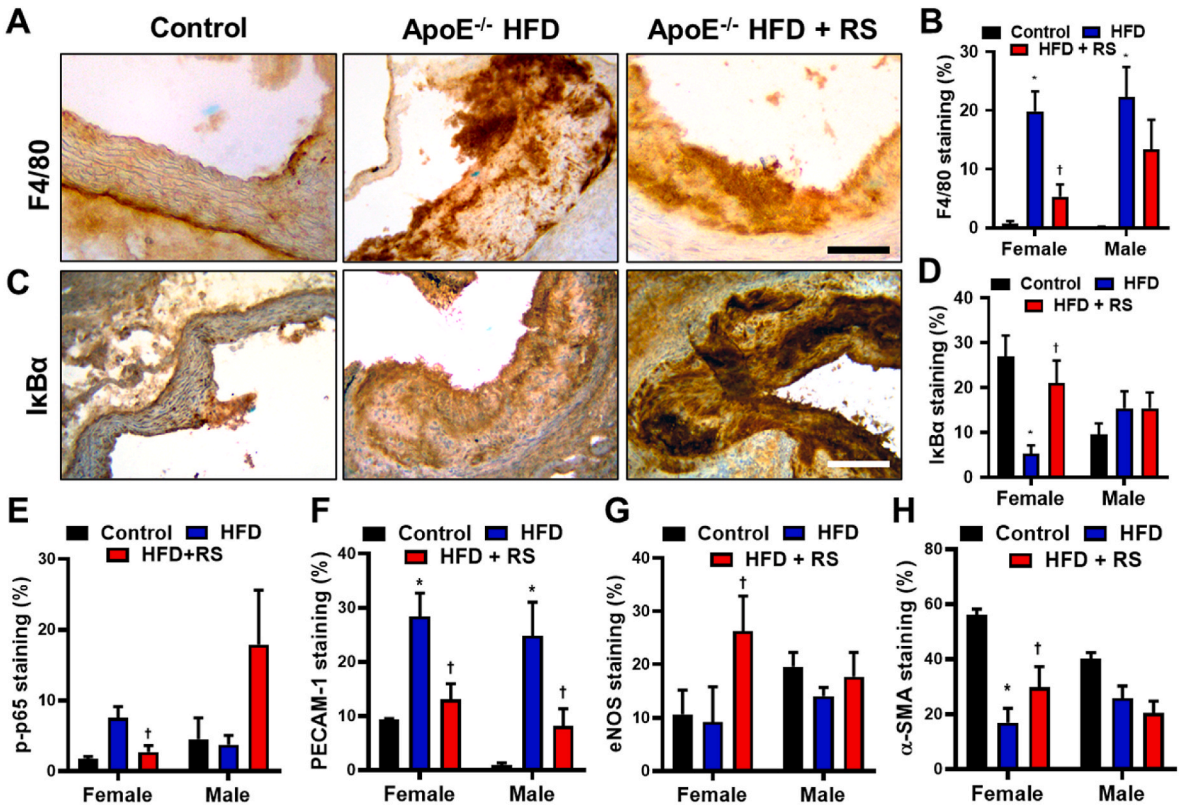

Fig. 7. Attenuation of inflammatory markers by RS in the aortic arch. (A) Aortic arch histology sections of female (shown) and male mice in the three groups were stained for F4/80. Scale bar = 100 μm. (B) In female mice treated with RS, there was a reduction of F4/80 positive staining (n = 7). $^{*}p = 0.0036$ female control vs ApoE$^{-/-}$ HFD, $^{\dagger}p = 0.0043$ female ApoE$^{-/-}$ HFD vs ApoE$^{-/-}$ HFD + RS, $^{*}p = 0.0325$ male control vs ApoE$^{-/-}$ HFD. (C) Aortic arch sections were also stained for IκBα. Scale bar = 100 μm. (D) There was an increase in IκBα positive staining in female ApoE$^{-/-}$ mice fed HFD with RS (n = 7). $^{*}p = 0.0147$ female control vs ApoE$^{-/-}$ HFD, $^{\dagger}p = 0.0281$ female ApoE$^{-/-}$ HFD vs ApoE$^{-/-}$ HFD + RS. (E) In female mice, phosphorylation of NF-κB/p65 also decreased with RS treatment (n = 7). $^{\dagger}p = 0.0386$ female ApoE$^{-/-}$ HFD vs ApoE$^{-/-}$ HFD + RS. (F) Positive staining for PECAM-1 was lower in female and male mice treated with RS (n = 7). $^{*}p = 0.0370$ female control vs ApoE$^{-/-}$ HFD, $^{\dagger}p = 0.0129$ female ApoE$^{-/-}$ HFD vs ApoE$^{-/-}$ HFD + RS, $^{*}p = 0.0106$ male control vs ApoE$^{-/-}$ HFD, $^{\dagger}p = 0.0217$ female ApoE$^{-/-}$ HFD vs ApoE$^{-/-}$ HFD + RS. Finally, in female mice, (G) eNOS and (H) α-SMA staining were increased with RS treatment (n = 7). For eNOS, $^{\dagger}p = 0.0406$ female ApoE$^{-/-}$ HFD vs ApoE$^{-/-}$ HFD + RS. For α-SMA, $^{*}p = 0.0028$ female control vs ApoE$^{-/-}$ HFD, $^{\dagger}p = 0.0320$ female ApoE$^{-/-}$ HFD vs ApoE$^{-/-}$ HFD + RS.

showed significant regulation in circadian rhythm related/regulated genes, liver inflammation or injury genes, or liver metabolism genes (Fig. 9E). Specifically, we saw upregulation in circadian rhythm-related genes by RS including PER3, a major regulator of the circadian rhythm in peripheral tissues [47]. In addition, there was a significant down regulation in several genes relating to liver inflammation. There were also major shifts in liver metabolism related genes in the female mice.

4. Discussion

Atherosclerosis is a chronic disease characterized by inflammation, lipid accumulation and the progressive development of plaques [1,2]. Lipid lowering therapies including statins have provided significant reductions in the risk of fatal coronary heart disease and non-fatal myocardial infarction. However, in spite of these advancements, atherosclerotic disease continues to be a pervasive clinical problem [48]. Atherosclerosis slowly progresses for life, placing more strict requirements on pharmaceutical products to treat vascular disease in comparison to many other diseases. Compounds for treating atherosclerosis will need to be taken orally by patients on a daily basis for decades, requiring long-term safety and representing a major investment by healthcare systems to provide for patients. Our studies demonstrate that rhamnan sulfate has potent anti-inflammatory properties, reduces vSMC proliferation and reduces atherosclerosis in a hyperlipidemic mouse model. As rhamnan sulfate is relatively inexpensive and has been consumed by millions of people as part of their diet, it would present an easily implementable adjuvant therapy to lipid lowering drugs and other treatments for atherosclerotic disease if it were effective in human patients.

Our studies indicate that rhamnan sulfate has atheroprotective effects though multiple modes of action. It reduces migration of vascular cells and binds to pro-growth and inflammatory growth factors with an affinity similar to that of heparin, suppressing the growth of vSMCs. Our studies suggest that this effect could proceed through binding of growth factors including FGF-2 and PDGF-BB. However, RS also inhibits migration in the absence of stimulation with these factors suggesting it may also act by directly altering cellular adhesion/migration mechanisms. The uptake of RS was reduced in both endothelial and vascular smooth muscle cells with rottlerin treatment. This indicates that a major mechanism of entry into the cells is macropinocytosis. In vSMCs, mitomycin treatment also reduced nuclear levels of RS, implying that RS may enter the nucleus during mitosis. This effect may be more pronounced in vSMCs due to their higher proliferation rate.

Our work indicates that rhamnan sulfate accumulates in vascular cells over the course of several days and is also deposited in the extracellular matrix. Interestingly, rhamnan sulfate appears to be able to access and bind to nuclear protein during cell division. This finding suggests a novel mechanism of action for RS, in which it accumulates in the cytoplasm of the cells followed by binding to nuclear proteins, including NF-κB, during cell division. The polyanionic structure of rhamnan sulfate may mimic that of DNA, allowing it to competitively bind to regions of proteins that bind to DNA. In comparison, heparin can facilitate the nuclear entry of growth factors but heparin and its antiproliferative derivatives do not enter the nucleus of vSMCs [49]. Prior

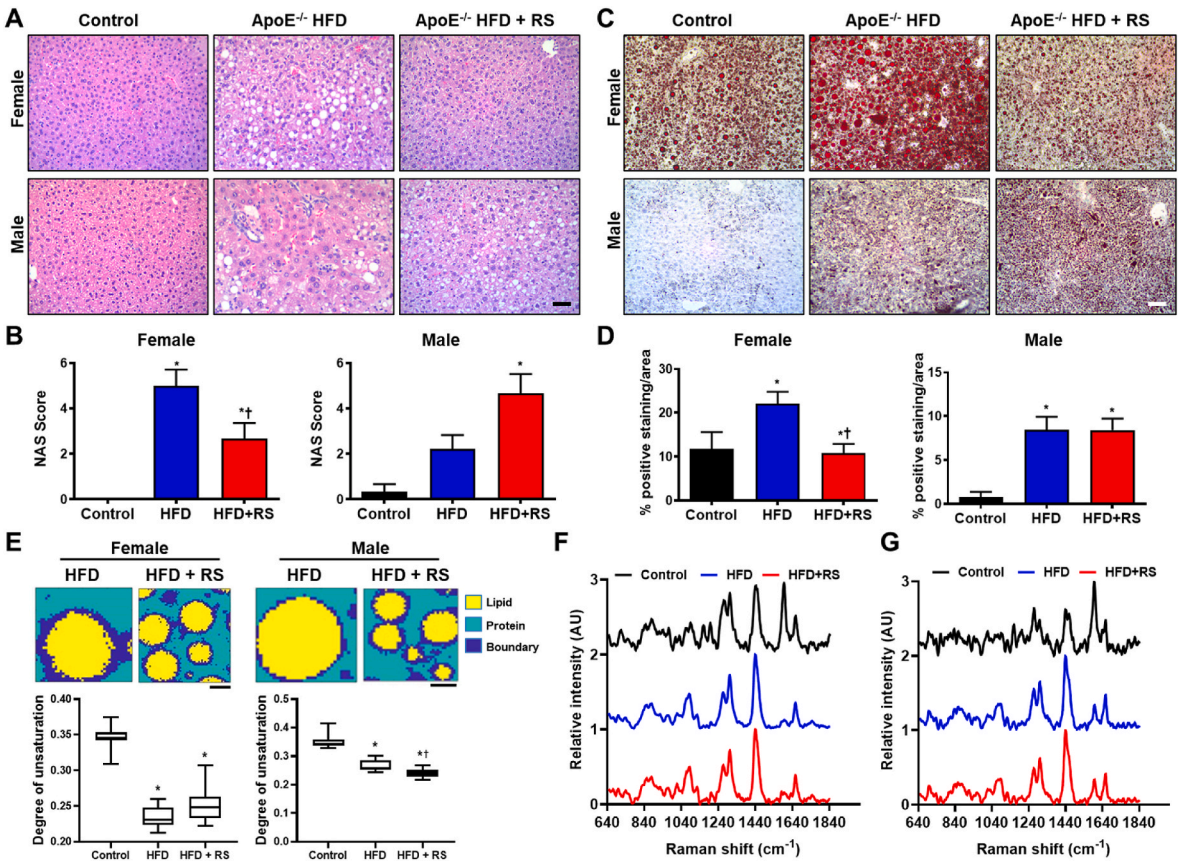

Fig. 8. Lipid deposition in the liver is attenuated with RS treatment *in vivo*. (A) Sections of liver from female and male mice were stained with hematoxylin and eosin. Scale bar = 300 μm. (B) Treatment with RS led to reduced NAS scores in female livers but did not change in male livers compared to mice on HFD (n = 10). $^{*}p = 0.0003$ female control vs ApoE$^{-/-}$ HFD, $^{*}p = 0.0475$ female control vs ApoE$^{-/-}$ HFD + RS, $^{\dagger}p = 0.0394$ female ApoE$^{-/-}$ HFD vs ApoE$^{-/-}$ HFD + RS, $^{*}p = 0.0186$ male control vs ApoE$^{-/-}$ HFD + RS. (C) Sections of liver from female and male mice were also stained with Oil Red-O. Scale bar = 300 μm. (D) Lipid deposition was decreased in livers from female mice but there was no change in livers of male mice treated with HFD + RS compared to those on HFD (n = 10). $^{\dagger}p = 0.0122$ female ApoE$^{-/-}$ HFD vs ApoE$^{-/-}$ HFD + RS, $^{*}p = 0.0094$ male control vs ApoE$^{-/-}$ HFD, $^{*}p = 0.0085$ male control vs ApoE$^{-/-}$ HFD + RS. (E) Raman spectroscopy imaging of livers from female mice showed no difference in lipid unsaturation between HFD and HFD + RS groups (n = 4). Scale bar = 10 μm $^{*}p < 0.0001$ control vs ApoE$^{-/-}$ HFD, $^{*}p < 0.0001$ control vs ApoE$^{-/-}$ HFD + RS. (F) Raman spectroscopy imaging of livers from male mice showed lower degree of lipid unsaturation in livers of mice treated with RS compared to HFD group (n = 3). Scale bar = 10 μm $^{*}p < 0.0001$ control vs ApoE$^{-/-}$ HFD, $^{*}p < 0.0001$ control vs ApoE$^{-/-}$ HFD + RS, $^{\dagger}p < 0.0001$ ApoE$^{-/-}$ HFD vs ApoE$^{-/-}$ HFD + RS. Average spectra of livers from (G) female and (H) male mice from the three groups. (For interpretation of the references to color in this figure legend, the reader is referred to the Web version of this article.)

studies have also suggested that the cellular localization of low molecular weight heparin is dependent on sulfation; however, none of the modified forms are found in the nucleus [50]. Thus, rhamnan sulfate is likely not simply acting as a heparin analogue in this activity. Although the role of the NF-κB pathway in atherosclerosis is complex, inhibition of the pathway would likely have net beneficial effects in treating atherosclerosis. Signaling through the canonical NF-κB pathway has been linked to proinflammatory signaling in atherosclerosis [51]. In addition, NF-κB signaling, in concert with other pathways, regulates expression of inflammatory, matrix metalloprotease (MMP) expression and cathepsins [51–57]. Inflammation and expression of proteases that degrade the extracellular matrix (ECM) are associated with vSMC hyperplasia, unstable plaque morphology and plaque rupture [58–61].

A striking feature of our findings is the differences in response between male and female animals treated with rhamnan sulfate. In the blood vessels in mice treated with rhamnan sulfate, at the aortic root there was a more pronounced reduction in lipid area for male mice, but the overall lesion and stenotic response was only significantly lower in females. In the thoracic aorta, only female mice had a reduction in plaque size and stenosis. We also observed a stronger cholesterol-lowering effect of rhamnan sulfate in female mice compared to male mice. Lipid lowering effects have been observed for marine polysaccharides including fucoidan, ulvan, and laminarin sulfate [62–64]. In comparison to these, rhamnan sulfate did not produce as dramatic reductions in lipids. The anti-inflammatory properties of rhamnan sulfate appeared to be stronger in female mice as well, including significant lowering of plaque inflammation and a marked reduction in the NAS score, inflammation and lipids with rhamnan sulfate treatment. Conversely, rhamnan sulfate treatment increased the NAS score in the liver of male mice and reduced the unsaturated lipids in the liver.

Several recent studies have shown that there is increased expression of lipid metabolism and transport genes in female humans and mice [65, 66]. Female mice are also more susceptible to developing non-alcoholic fatty liver disease and have increased inflammation in the liver in comparison to male mice under similar treatments [67]. Our study also showed baseline differences in the liver of mice under a high fat diet based on sex, with female mice having higher NAS scores and lipid content in the liver compared to male mice. Thus, the anti-inflammatory properties of rhamnan sulfate may benefit female mice more greatly since they have increased inflammation in liver in response to the high fat diet. Our studies examining the gene expression in the liver of the mice treated with a high fat diet supported the notion that RS reduces liver inflammation and regulated circadian rhythm related genes. These effects were more significant in the female mice and there were differences in the regulation of metabolic genes that was sex-specific in response to RS treatment. The mechanisms of liver steatosis are

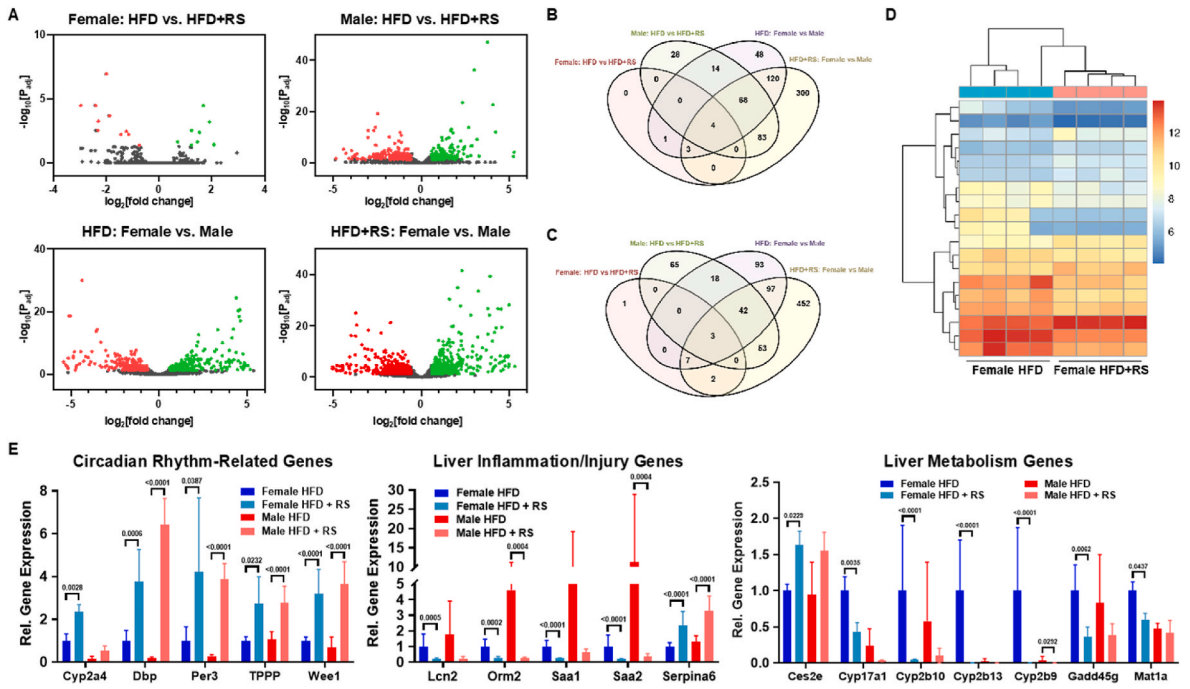

Fig. 9. Analysis of RNA expression in liver of mice. (A) Volcano plots of differential gene expression comparing between the groups. Genes with significant upregulation shown in green and downregulation shown in red. (B) Venn diagram of genes that are significantly upregulated in the groups. (C) Venn diagram of genes that are significantly downregulated in the groups. (D) Clustering analysis of female mice with our without RS treatment. (E) Changes in individual genes that were in common for the groups (n = 4). *$p < 0.05$ versus the respective non-RS treated group for male or female mice. (For interpretation of the references to color in this figure legend, the reader is referred to the Web version of this article.)

multi-factorial and the mechanisms of NAFLD/NASH are not completely understood [68]. They involve, among other pathways, the regulation of CLOCK genes, liver inflammation and lipid metabolism. These processes were altered in our studies for the liver in the RNA seq analysis. Adipose tissue deposition involved the uptake of lipids from the blood and RS had only a moderate effect on the blood lipid levels. Thus, the difference in these findings is likely due to the effects of RS specifically on liver gene expression and lack of a strong effect on blood lipids.

Overall, our studies demonstrate that rhamnan sulfate can provide significant benefits for inhibiting the development of atherosclerosis and acts though multiple mechanisms including the reduction of inflammation, inhibition of vascular cell proliferation and enhanced endothelial barrier function. Due to the low cost and ease of availability, RS may have high potential as an easily implementable adjunct therapy for atherosclerosis. Our studies used a highly purified form of rhamnan sulfate, which may allow it to have increased binding capacity and activity in comparison to less pure forms. Further studies would be needed to determine if less purified forms of the compound have similar activity and if particular subfractions of RS can be linked to specific mechanistic activities.

Author contributions

N·P·P., A.G.-H., M.W.M., F.Z., L.C., X.F., L.Y., K.X., E.T., E.Y·Y., V.L., M.E.F., J. Tunnell, J. Tarbell, R.J.L. and A.B.B. performed experiments, processed and analyzed data. A.G.-R. and C.G.-M. analyzed and scored histological sections. J.L., A.G.-H., and A.B.B. wrote and edited the manuscript. A.B.B. initiated the project and oversaw all aspects of the project. All authors reviewed and approved the manuscript before publication.

Declaration of competing interest

The authors declare the following financial interests/personal relationships which may be considered as potential competing interests: Aaron Baker reports financial support was provided by National Institutes of Health. Aaron Baker reports financial support was provided by US Office of Congressionally Directed Medical Research Programs. Aaron Baker reports financial support was provided by American Heart Association. Robert Linhardt reports financial support was provided by National Institutes of Health.

Data availability

Data will be made available on request.

Acknowledgements

The authors gratefully acknowledge funding though the American Heart Association (17IRG33410888), the DOD CDMRP (W81XWH-16-1-0580; W81XWH-16-1-0582) and the National Institutes of Health (1R21EB023551-01; 1R21EB024147-01A1; 1R01HL141761-01) to ABB. This work was funded by National Institutes of Health Grants DK111958, CA231074, NS088496 and AG062344 to RJL.

Appendix A. Supplementary data

Supplementary data to this article can be found online at https://doi.org/10.1016/j.biomaterials.2022.121865.

References

[1] H.C. Stary, A.B. Chandler, S. Glagov, J.R. Guyton, W. Insull Jr., M.E. Rosenfeld, S. A. Schaffer, C.J. Schwartz, W.D. Wagner, R.W. Wissler, A definition of initial, fatty streak, and intermediate lesions of atherosclerosis. A report from the Committee on Vascular Lesions of the Council on Arteriosclerosis, American Heart Association, Circulation 89 (5) (1994) 2462–2478.
[2] L.B. Nielsen, Transfer of low density lipoprotein into the arterial wall and risk of atherosclerosis, Atherosclerosis 123 (1–2) (1996) 1–15.
[3] R. Bitzur, H. Cohen, Y. Kamari, D. Harats, Intolerance to statins: mechanisms and management, Diabetes Care 36 (Supplement 2) (2013) S325–S330.

[4] N.C. Ward, G.F. Watts, R.H. Eckel, Statin toxicity: mechanistic insights and clinical implications, Circ. Res. 124 (2) (2019) 328–350.
[5] S. Weinbaum, J.M. Tarbell, E.R. Damiano, The structure and function of the endothelial glycocalyx layer, Annu. Rev. Biomed. Eng. 9 (2007) 121–167.
[6] C.S. Alphonsus, R.N. Rodseth, The endothelial glycocalyx: a review of the vascular barrier, Anaesthesia 69 (7) (2014) 777–784.
[7] B.M. van den Berg, H. Vink, J.A. Spaan, The endothelial glycocalyx protects against myocardial edema, Circ. Res. 92 (6) (2003) 592–594.
[8] P.L. Voyvodic, D. Min, R. Liu, E. Williams, V. Chitalia, A.K. Dunn, A.B. Baker, Loss of syndecan-1 induces a pro-inflammatory phenotype in endothelial cells with a dysregulated response to atheroprotective flow, J. Biol. Chem. 289 (14) (2014) 9547–9559.
[9] B.M. van den Berg, J.A. Spaan, H. Vink, Impaired glycocalyx barrier properties contribute to enhanced intimal low-density lipoprotein accumulation at the carotid artery bifurcation in mice, Pflueg. Arch. Eur. J. Physiol. 457 (6) (2009) 1199–1206.
[10] A.A. Constantinescu, H. Vink, J.A. Spaan, Endothelial cell glycocalyx modulates immobilization of leukocytes at the endothelial surface, Arterioscler. Thromb. Vasc. Biol. 23 (9) (2003) 1541–1547.
[11] A.W. Mulivor, H.H. Lipowsky, Inflammation- and ischemia-induced shedding of venular glycocalyx, Am. J. Physiol. Heart Circ. Physiol. 286 (5) (2004) H1672–H1680.
[12] S. Devaraj, J.M. Yun, G. Adamson, J. Galvez, I. Jialal, C-reactive protein impairs the endothelial glycocalyx resulting in endothelial dysfunction, Cardiovasc. Res. 84 (3) (2009) 479–484.
[13] S.V. Lopez-Quintero, L.M. Cancel, A. Pierides, D. Antonetti, D.C. Spray, J. M. Tarbell, High glucose attenuates shear-induced changes in endothelial hydraulic conductivity by degrading the glycocalyx, PLoS One 8 (11) (2013), e78954.
[14] M. Gouverneur, B. Berg, M. Nieuwdorp, E. Stroes, H. Vink, Vasculoprotective properties of the endothelial glycocalyx: effects of fluid shear stress, J. Intern. Med. 259 (4) (2006) 393–400.
[15] T. Rademakers, K. Douma, T.M. Hackeng, M.J. Post, J.C. Sluimer, M.J. Daemen, E. A. Biessen, S. Heeneman, M.A. van Zandvoort, Plaque-associated vasa vasorum in aged apolipoprotein E-deficient mice exhibit proatherogenic functional features in vivo, Arterioscler. Thromb. Vasc. Biol. 33 (2) (2013) 249–256.
[16] B.M. van den Berg, J.A. Spaan, T.M. Rolf, H. Vink, Atherogenic region and diet diminish glycocalyx dimension and increase intima-to-media ratios at murine carotid artery bifurcation, Am. J. Physiol. Heart Circ. Physiol. 290 (2) (2006) H915–H920.
[17] H. Vink, A.A. Constantinescu, J.A. Spaan, Oxidized lipoproteins degrade the endothelial surface layer : implications for platelet-endothelial cell adhesion, Circulation 101 (13) (2000) 1500–1502.
[18] E.P. Schmidt, Y. Yang, W.J. Janssen, A. Gandjeva, M.J. Perez, L. Barthel, R. L. Zemans, J.C. Bowman, D.E. Koyanagi, Z.X. Yunt, L.P. Smith, S.S. Cheng, K. H. Overdier, K.R. Thompson, M.W. Geraci, I.S. Douglas, D.B. Pearse, R.M. Tuder, The pulmonary endothelial glycocalyx regulates neutrophil adhesion and lung injury during experimental sepsis, Nat. Med. 18 (8) (2012) 1217–1223.
[19] M. Rehm, S. Zahler, M. Lotsch, U. Welsch, P. Conzen, M. Jacob, B.F. Becker, Endothelial glycocalyx as an additional barrier determining extravasation of 6% hydroxyethyl starch or 5% albumin solutions in the coronary vascular bed, Anesthesiology 100 (5) (2004) 1211–1223.
[20] A.W. Mulivor, H.H. Lipowsky, Role of glycocalyx in leukocyte-endothelial cell adhesion, Am. J. Physiol. Heart Circ. Physiol. 283 (4) (2002) H1282–H1291.
[21] P. Laurienzo, Marine polysaccharides in pharmaceutical applications: an overview, Mar. Drugs 8 (9) (2010) 2435–2465.
[22] N.P. Patil, V. Le, A.D. Sligar, L. Mei, D. Chavarria, E.Y. Yang, A.B. Baker, Algal polysaccharides as therapeutic agents for atherosclerosis, Frontiers in cardiovascular medicine 5 (2018) 153.
[23] S. Patel, Therapeutic importance of sulfated polysaccharides from seaweeds: updating the recent findings, 3 Biotech 2 (3) (2012) 171–185.
[24] N. Li, X. Liu, X. He, S. Wang, S. Cao, Z. Xia, H. Xian, L. Qin, W. Mao, Structure and anticoagulant property of a sulfated polysaccharide isolated from the green seaweed Monostroma angicava, Carbohydr. Polym. 159 (2017) 195–206.
[25] T. Okamoto, N. Akita, M. Terasawa, T. Hayashi, K. Suzuki, Rhamnan sulfate extracted from Monostroma nitidum attenuates blood coagulation and inflammation of vascular endothelial cells, J. Nat. Med. 73 (3) (2019) 614–619.
[26] L. Zang, Y. Shimada, T. Tanaka, N. Nishimura, Rhamnan sulphate from Monostroma nitidum attenuates hepatic steatosis by suppressing lipogenesis in a diet-induced obesity zebrafish model, J. Funct.Foods 17 (2015) 364–370.
[27] X. Liu, S. Wang, S. Cao, X. He, L. Qin, M. He, Y. Yang, J. Hao, W. Mao, Structural characteristics and anticoagulant property in vitro and in vivo of a seaweed sulfated rhamnan, Mar. Drugs 16 (7) (2018) 243.
[28] C.G. Glabe, P.K. Harty, S.D. Rosen, Preparation and properties of fluorescent polysaccharides, Anal. Biochem. 130 (2) (1983) 287–294.
[29] L.M. Cancel, J.M. Tarbell, The role of apoptosis in LDL transport through cultured endothelial cell monolayers, Atherosclerosis 208 (2) (2010) 335–341.
[30] L.M. Cancel, A. Fitting, J.M. Tarbell, In vitro study of LDL transport under pressurized (convective) conditions, Am. J. Physiol. Heart Circ. Physiol. 293 (1) (2007) H126–H132.
[31] Y. Zeng, E.E. Ebong, B.M. Fu, J.M. Tarbell, The structural stability of the endothelial glycocalyx after enzymatic removal of glycosaminoglycans, PLoS One 7 (8) (2012).
[32] S. Pillarisetti, L. Paka, J.C. Obunike, L. Berglund, I.J. Goldberg, Subendothelial retention of lipoprotein (a). Evidence that reduced heparan sulfate promotes lipoprotein binding to subendothelial matrix, J. Clin. Invest. 100 (4) (1997) 867–874.
[33] D.E. Kleiner, E.M. Brunt, M. Van Natta, C. Behling, M.J. Contos, O.W. Cummings, L. D. Ferrell, Y.C. Liu, M.S. Torbenson, A. Unalp-Arida, Design and validation of a histological scoring system for nonalcoholic fatty liver disease, Hepatology 41 (6) (2005) 1313–1321.
[34] E.M. Brunt, C.G. Janney, A.M. Di Bisceglie, B.A. Neuschwander-Tetri, B.R. Bacon, Nonalcoholic steatohepatitis: a proposal for grading and staging the histological lesions, Am. J. Gastroenterol. 94 (9) (1999) 2467–2474.
[35] X. Feng, A.J. Moy, H.T.M. Nguyen, J. Zhang, M.C. Fox, K.R. Sebastian, J. S. Reichenberg, M.K. Markey, J.W. Tunnell, Raman active components of skin cancer, Biomed. Opt Express 8 (6) (2017) 2835–2850.
[36] K. Kochan, E. Maslak, C. Krafft, R. Kostogrys, S. Chlopicki, M. Baranska, Raman spectroscopy analysis of lipid droplets content, distribution and saturation level in Non-Alcoholic Fatty Liver Disease in mice, J. Biophot. 8 (7) (2015) 597–609.
[37] K. Kochan, K.M. Marzec, K. Chruszcz-Lipska, A. Jasztal, E. Maslak, H. Musiolik, S. Chłopicki, M. Baranska, Pathological changes in the biochemical profile of the liver in atherosclerosis and diabetes assessed by Raman spectroscopy, Analyst 138 (14) (2013) 3885–3890.
[38] S.Y. Kim, F. Zhang, W. Gong, K. Chen, K. Xia, F. Liu, R. Gross, J.M. Wang, R. J. Linhardt, M.L. Cotten, Copper regulates the interactions of antimicrobial piscidin peptides from fish mast cells with formyl peptide receptors and heparin, J. Biol. Chem. 293 (40) (2018) 15381–15396.
[39] A. Rudijanto, The role of vascular smooth muscle cells on the pathogenesis of atherosclerosis, Acta Med. Indones. 39 (2) (2007) 86–93.
[40] L. Lamalice, F. Le Boeuf, J. Huot, Endothelial cell migration during angiogenesis, Circ. Res. 100 (6) (2007) 782–794.
[41] M.A. Gimbrone Jr., G. García-Cardeña, Endothelial cell dysfunction and the pathobiology of atherosclerosis, Circ. Res. 118 (4) (2016) 620–636.
[42] X.-H. Yu, X.-L. Zheng, C.-K. Tang, Nuclear Factor-Kb Activation as a Pathological Mechanism of Lipid Metabolism and Atherosclerosis, 2015.
[43] R. Gareus, E. Kotsaki, S. Xanthoulea, I. van der Made, M.J. Gijbels, R. Kardakaris, A. Polykratis, G. Kollias, M.P. de Winther, M. Pasparakis, Endothelial cell-specific NF-kappaB inhibition protects mice from atherosclerosis, Cell Metabol. 8 (5) (2008) 372–383.
[44] S. Kawashima, M. Yokoyama, Dysfunction of endothelial nitric oxide synthase and atherosclerosis, Arterioscler. Thromb. Vasc. Biol. 24 (6) (2004) 998–1005.
[45] Y.Y. Zhou, X.D. Zhou, S.J. Wu, D.H. Fan, S. Van Poucke, Y.P. Chen, S.W. Fu, M. H. Zheng, Nonalcoholic fatty liver disease contributes to subclinical atherosclerosis: a systematic review and meta-analysis, Hepatology communications 2 (4) (2018) 376–392.
[46] R.S. Muhammad, N. Abu-Saleh, S. Kinaneh, M. Agbaria, E. Sabo, C. Grajeda-Iglesias, N. Volkova, S. Hamoud, Heparanase inhibition attenuates atherosclerosis progression and liver steatosis in E0 mice, Atherosclerosis 276 (2018) 155–162.
[47] S.N. Archer, C. Schmidt, G. Vandewalle, D.J. Dijk, Phenotyping of PER3 variants reveals widespread effects on circadian preference, sleep regulation, and health, Sleep Med. Rev. 40 (2018) 109–126.
[48] F. Taylor, M.D. Huffman, A.F. Macedo, T.H. Moore, M. Burke, G. Davey Smith, K. Ward, S. Ebrahim, Statins for the primary prevention of cardiovascular disease, Cochrane Database Syst. Rev. 1 (2013) CD004816.
[49] T. Barzu, M. Pascal, M. Maman, C. Roque, F. Lafont, A. Rousselet, Entry and distribution of fluorescent antiproliferative heparin derivatives into rat vascular smooth muscle cells: comparison between heparin-sensitive and heparin-resistant cultures, J. Cell. Physiol. 167 (1) (1996) 8–21.
[50] K. Raman, C. Mencio, U.R. Desai, B. Kuberan, Sulfation patterns determine cellular internalization of heparin-like polysaccharides, Mol. Pharm. 10 (4) (2013) 1442–1449.
[51] C. Monaco, E. Andreakos, S. Kiriakidis, C. Mauri, C. Bicknell, B. Foxwell, N. Cheshire, E. Paleolog, M. Feldmann, Canonical pathway of nuclear factor kappa B activation selectively regulates proinflammatory and prothrombotic responses in human atherosclerosis, Proc. Natl. Acad. Sci. U. S. A. 101 (15) (2004) 5634–5639.
[52] S. Alam, Q. Liu, S. Liu, Y. Liu, Y. Zhang, X. Yang, G. Liu, K. Fan, J. Ma, Up-regulated cathepsin C induces macrophage M1 polarization through FAK-triggered p38 MAPK/NF-kappaB pathway, Exp. Cell Res. 382 (2) (2019), 111472.
[53] Y.J. Chen, L.S. Chang, NFkappaB- and AP-1-mediated DNA looping regulates matrix metalloproteinase-9 transcription in TNF-alpha-treated human leukemia U937 cells, Biochim. Biophys. Acta 1849 (10) (2015) 1248–1259.
[54] S. Ferre, E. Baldoli, M. Leidi, J.A. Maier, Magnesium deficiency promotes a pro-atherogenic phenotype in cultured human endothelial cells via activation of NFkB, Biochim. Biophys. Acta 1802 (11) (2010) 952–958.
[55] R.W. Guo, L.X. Yang, H. Wang, B. Liu, L. Wang, Angiotensin II induces matrix metalloproteinase-9 expression via a nuclear factor-kappaB-dependent pathway in vascular smooth muscle cells, Regul. Pept. 147 (1–3) (2008) 37–44.
[56] X.L. Wang, Y.L. Zhou, W. Sun, L. Li, Rosuvastatin attenuates cd40l-induced downregulation of extracellular matrix production in human aortic smooth muscle cells via TRAF6-JNK-NF-kappaB pathway, PLoS One 11 (4) (2016), e0153919.
[57] J. Yu, G. Sun, Y. Chen, L. Li, H. Wang, D. Tu, L. Li, Z. Meng, Y. Wang, CEACAM1 inhibited IkappaB-alpha/NF-kappaB signal pathway via targeting MMP-9/TIMP-1 Axis in diabetic atherosclerosis, J. Cardiovasc. Pharmacol. 76 (3) (2020) 329–336.
[58] A.B. Baker, Y.S. Chatzizisis, R. Beigel, M. Jonas, B.V. Stone, A.U. Coskun, C. Maynard, C. Rogers, K.C. Koskinas, C.L. Feldman, P.H. Stone, E.R. Edelman, Regulation of heparanase expression in coronary artery disease in diabetic, hyperlipidemic swine, Atherosclerosis 213 (2) (2010) 436–442.
[59] Y.S. Chatzizisis, A.B. Baker, G.K. Sukhova, K.C. Koskinas, M.I. Papafaklis, R. Beigel, M. Jonas, A.U. Coskun, B.V. Stone, C. Maynard, G.P. Shi, P. Libby, C.L. Feldman, E. R. Edelman, P.H. Stone, Augmented expression and activity of extracellular matrix-degrading enzymes in regions of low endothelial shear stress colocalize with

coronary atheromata with thin fibrous caps in pigs, Circulation 123 (6) (2011) 621–630.
[60] P. Libby, Inflammation during the life cycle of the atherosclerotic plaque, Cardiovasc. Res. 117 (13) (2021) 2525–2536.
[61] H. Wang, X. Meng, L. Piao, A. Inoue, W. Xu, C. Yu, K. Nakamura, L. Hu, T. Sasaki, H. Wu, K. Unno, H. Umegaki, T. Murohara, G.P. Shi, M. Kuzuya, X.W. Cheng, Cathepsin S deficiency mitigated chronic stress-related neointimal hyperplasia in mice, J. Am. Heart Assoc. 8 (14) (2019), e011994.
[62] T. Zaporozhets, N. Besednova, Prospects for the therapeutic application of sulfated polysaccharides of brown algae in diseases of the cardiovascular system, Pharmaceut. Biol. 54 (12) (2016) 3126–3135.
[63] S. Hassan, S.A. El-Twab, M. Hetta, B. Mahmoud, Improvement of lipid profile and antioxidant of hypercholesterolemic albino rats by polysaccharides extracted from the green alga Ulva lactuca Linnaeus, Saudi J. Biol. Sci. 18 (4) (2011) 333–340.
[64] E. Besterman, Effects of laminarin sulphate on experimental atherosclerosis and on serum lipids in rabbits during long-term intermittent cholesterol feeding, Atherosclerosis 12 (1) (1970) 85–96.
[65] Y. Zhang, K. Klein, A. Sugathan, N. Nassery, A. Dombkowski, U.M. Zanger, D. J. Waxman, Transcriptional profiling of human liver identifies sex-biased genes associated with polygenic dyslipidemia and coronary artery disease, PLoS One 6 (8) (2011), e23506.
[66] A. Sugathan, D.J. Waxman, Genome-wide analysis of chromatin states reveals distinct mechanisms of sex-dependent gene regulation in male and female mouse liver, Mol. Cell Biol. 33 (18) (2013) 3594–3610.
[67] A. Spruss, J. Henkel, G. Kanuri, D. Blank, G.P. Puschel, S.C. Bischoff, I. Bergheim, Female mice are more susceptible to nonalcoholic fatty liver disease: sex-specific regulation of the hepatic AMP-activated protein kinase-plasminogen activator inhibitor 1 cascade, but not the hepatic endotoxin response, Mol. Med. 18 (2012) 1346–1355.
[68] F. Bessone, M.V. Razori, M.G. Roma, Molecular pathways of nonalcoholic fatty liver disease development and progression, Cell. Mol. Life Sci. 76 (1) (2019) 99–128.